The Ericksen model of liquid crystals with colloidal and electric effects

Ricardo H. Nochetto [a], Shawn W. Walker [b],[*], Wujun Zhang [c]

[a] Department of Mathematics and Institute for Physical Science and Technology, University of Maryland, College Park, MD 20742, United States
[b] Department of Mathematics and Center for Computation and Technology (CCT) Louisiana State University, Baton Rouge, LA 70803, United States
[c] Department of Mathematics, Rutgers University, Piscataway, NJ 08854, United States

ARTICLE INFO

ABSTRACT

We present a robust discretization of the Ericksen model of liquid crystals with variable degree of orientation coupled with colloidal effects and electric fields. The total energy consists of the Ericksen energy, a weak anchoring (or penalized Dirichlet) energy to model colloids, and an electrical energy for a given electric field. We describe our special discretization of the total energy along with a method to compute minimizers via a discrete quasi-gradient flow algorithm which has a strictly monotone energy decreasing property. Numerical experiments are given in two and three dimensions to illustrate that the method is able to capture non-trivial defect patterns, such as the Saturn ring defect. We conclude with a rigorous proof of the Γ-convergence of our discrete energy to the continuous energy.
© 2017 Elsevier Inc. All rights reserved.

1. Introduction

This paper presents a method for solving the Ericksen model of liquid crystals [1,2], with additional effects due to colloidal domains and electric fields. Liquid crystals are a work-horse technology enabling electronic displays [3–5], for instance. Moreover, they have a host of potential applications in material science [6–21]. One avenue is to use external fields (e.g. electric fields) and colloidal dispersions to build new materials through directed self-assembly [22,7,12,23–29,16, 19,30,31].

A significant amount of mathematical analysis has been done on liquid crystals [32–44]. Moreover, a host of numerical methods have been developed for statics and dynamics [45–51]. In particular, the methods in [52,43,53–55] are for harmonic mappings and liquid crystals with fixed degree of orientation, i.e. a unit vector field $\mathbf{n}$ (called the director field) represents the orientation of liquid crystal molecules. See [56–60] for methods that couple liquid crystals to Stokes flow. We also refer to the survey paper [45] for more numerical methods.

The method we present [61,62] is for the one-constant model of liquid crystals with variable degree of orientation [1,2, 32] (Ericksen's model). The state of the liquid crystal is described by a director field $\mathbf{n}$ and a scalar function s, the so-called degree-of-orientation, which minimize the energy

$$E[s, \mathbf{n}] := \int_\Omega \left(\kappa |\nabla s|^2 + s^2 |\nabla \mathbf{n}|^2 \right) dx + \int_\Omega \psi(s) dx. \tag{1}$$

* Corresponding author.
E-mail addresses: rhn@math.umd.edu (R.H. Nochetto), walker@math.lsu.edu (S.W. Walker), wujun@math.rutgers.edu (W. Zhang).
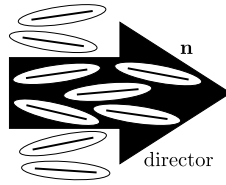
Fig. 1. Macroscopic order parameter: the director variable **n**. Nematic liquid crystal molecules have an elongated rod-like shape (see elongated ellipsoids), which gives the material its *anisotropic* nature. The value of **n**(*x*) (a unit vector), at the point *x*, represents a probabilistic average over a local ensemble of liquid crystal molecules "near" *x* [32].

Hereafter, $\kappa > 0$ is a material constant, Ω is a bounded Lipschitz domain in $\mathbb{R}^d$ with $d \geq 2$, and ψ is a double well potential (defined below).

Minimizers of the Ericksen model may exhibit non-trivial defects (depending on boundary conditions) [63,10,64,39,38, 65]. The presence of s in (1) leads to an Euler–Lagrange equation for **n** that is *degenerate*. This allows for line and plane defects (singularities of **n**) in dimension $d = 3$ when s vanishes; these types of defects are important for applications, especially defects that lie on three dimensional space curves [7,66]. Regularity properties of minimizers, and the size of defects, were studied in [39]. This leads to the study of dynamics [33] and corresponding numerics [46], which are relevant to our paper. But in both cases they regularize the model to avoid the degeneracy associated with the order parameter s vanishing.

Our finite element method (FEM) does *not* require any regularization. We discussed the mathematical foundation of our method in [61,62]: we proved stability and convergence properties via Γ-convergence [67] (as the mesh size h goes to zero) and developed a quasi-gradient flow method to solve the discrete problem. Our discretization of the energy (1), defined in (16), requires that the mesh $\mathcal{T}_h$ be *weakly acute* (or the stronger condition of having *non-obtuse* angles). This discretization preserves the underlying structure and robustly handles the unit length constraint on **n** and the degeneracy present when s vanishes. Our previous paper [61] showed a variety of simulations of minimizers with interesting defect structures.

The present paper demonstrates the ability of the Ericksen model, and of our method, to capture defect structures induced by colloidal inclusions (i.e. holes in the domain) and effects due to electric fields. We are able to recreate the famous Saturn ring defect [68], which occurs around colloidal particles in different situations, by using both a conforming (non-obtuse mesh) and a non-conforming cube mesh with an immersed boundary approach to model the colloid. In addition, we include electric field effects by incorporating an electric energy term into the total energy (1), and demonstrate the classic *Freedericksz transition* [32,2,41,69,70]. We also investigate the coupling of colloidal and electric effects.

The paper is organized as follows. In Section 2, we recall the Ericksen model for liquid crystals with variable degree of orientation, and describe our discretization of the continuous energy. Section 3 recalls properties of the discretization, and our initial minimization scheme. Section 4 describes the details for properly implementing our method. Section 5.1 illustrates our method in the presence of a colloidal inclusion with a *conforming non-obtuse* mesh. Section 5.2 shows an alternative way to model colloids by an immersed boundary approach (along with supporting simulations). In Section 6, we show how to include electric field effects in the model and describe a modified minimization procedure to compute minimizers. Section 7 presents the monotone energy decreasing property of the quasi-gradient flow algorithm to compute discrete minimizers. Section 8 provides a summary of the Γ-convergence for our discrete energy. We close in Section 9 with some discussion.

2. Ericksen's model

Let the *director* field $\mathbf{n} : \Omega \subset \mathbb{R}^d \to \mathbb{S}^{d-1}$ be a vector-valued function with unit length (see Fig. 1 for a description of the meaning of **n**). The *degree-of-orientation* $s : \Omega \subset \mathbb{R}^d \to (-\frac{1}{2}, 1)$ is a real valued function (see Fig. 2 for a description of the meaning of s). The variable **n**, by itself, cannot properly describe a "loss of order" in the liquid crystal material because it has unit length. The s variable provides a way to characterize the local order (see Fig. 2).

2.1. Ericksen's one constant energy

The equilibrium state of the liquid crystal material is described by the pair $(s, \mathbf{n})$ minimizing a bulk-energy functional (1) which we split as

$$E_1[s, \mathbf{n}] := \int_\Omega \left(\kappa |\nabla s|^2 + s^2 |\nabla \mathbf{n}|^2 \right) dx, \qquad E_2[s] := \int_\Omega \psi(s) dx, \tag{2}$$

where $\kappa > 0$. The double well potential ψ is a C^2 function defined on $-1/2 < s < 1$ that satisfies [1,35,39]

1. $\lim_{s \to 1} \psi(s) = \lim_{s \to -1/2} \psi(s) = \infty$,
2. $\psi(0) > \psi(s^*) = \min_{s \in [-1/2, 1]} \psi(s) = 0$ for some $s^* \in (0, 1)$,
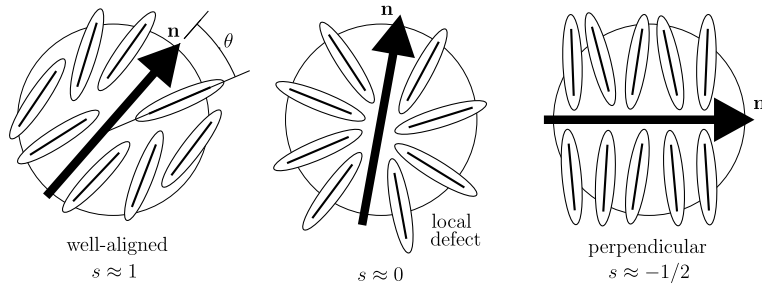3. $\psi'(0) = 0$.

Fig. 2. Macroscopic order parameter: the degree-of-orientation variable s. It is a probabilistic average over the angle θ between $\mathbf{n}(x)$ and an individual liquid crystal molecule; the average is taken over a local ensemble [32]. The case $s = 1$ represents the state of perfect alignment in which all molecules (in the ensemble) are parallel to $\mathbf{n}$. Likewise, $s = -1/2$ represents the state of microscopic order in which all molecules (in the ensemble) are perpendicular to $\mathbf{n}$. When $s = 0$, the molecules do not lie along any preferred direction which represents the state of an isotropic, uniformly random, distribution of molecules (in the ensemble). The state $s = 0$ is called a *defect* in the liquid crystal material.

It was shown in [35,39] that introducing an auxiliary variable $\mathbf{u} = s\mathbf{n}$ allows the energy $E_1[s, \mathbf{n}]$ to be rewritten as

$$E_1[s, \mathbf{n}] = \widetilde{E}_1[s, \mathbf{u}] := \int_\Omega \Big((\kappa - 1)|\nabla s|^2 + |\nabla \mathbf{u}|^2 \Big) dx, \tag{3}$$

which follows from the orthogonal decomposition $\nabla \mathbf{u} = \mathbf{n} \otimes \nabla s + s\nabla \mathbf{n}$ (and is due to the constraint $|\mathbf{n}| = 1$). Hence, [35,39] define the admissible class of solutions (minimizers) as

$$\mathbb{A} := \{(s, \mathbf{u}) : \Omega \to (-1/2, 1) \times \mathbb{R}^d : (s, \mathbf{u}) \in [H^1(\Omega)]^{d+1}, \ \mathbf{u} = s\mathbf{n}, \mathbf{n} \in \mathbb{S}^{d-1}\}. \tag{4}$$

We may also enforce boundary conditions on $(s, \mathbf{u})$, possibly on different parts of the boundary. Let $(\Gamma_s, \Gamma_\mathbf{u})$ be open subsets of $\partial\Omega$ where we set Dirichlet boundary conditions for $(s, \mathbf{u})$. Then we have the following restricted admissible class

$$\mathbb{A}(g, \mathbf{r}) := \Big\{ (s, \mathbf{u}) \in \mathbb{A} : \ s|_{\Gamma_s} = g, \quad \mathbf{u}|_{\Gamma_\mathbf{u}} = \mathbf{r} \Big\}, \tag{5}$$

for some given functions $(g, \mathbf{r}) \in [W^1_\infty(\mathbb{R}^d)]^{d+1}$ that satisfy the following in a neighborhood of $\partial\Omega$: $-1/2 < g < 1$ and $\mathbf{r} = g\mathbf{q}$, for some $\mathbf{q} \in \mathbb{S}^{d-1}$. Note that if we further assume

$$g \geq \delta_0 \quad \text{on } \partial\Omega, \ \text{for some } \delta_0 > 0, \tag{6}$$

then the function $\mathbf{n}$ is H^1 in a neighborhood of $\partial\Omega$ and satisfies $\mathbf{n} = g^{-1}\mathbf{r} = \mathbf{q} \in \mathbb{S}^{d-1}$ on $\partial\Omega$.

When the degree of orientation s is a non-zero constant, the energy $E_1[s, \mathbf{n}]$ in (2) effectively reduces to the Oseen-Frank energy $\int_\Omega |\nabla\mathbf{n}|^2$. The purpose of the degree of orientation is to relax the energy of defects. In fact, discontinuities in $\mathbf{n}$ (i.e. defects) may still occur in the singular set

$$\mathbb{S} := \{x \in \Omega : s(x) = 0\}, \tag{7}$$

with finite energy: $E[s, \mathbf{n}] < \infty$. The existence of minimizers in the admissible class, subject to Dirichlet boundary conditions, was shown in [35,39]. Minimizers with defects are constructed explicitly in [32] or discovered numerically in [61].

The parameter κ in (2) plays a major role in the occurrence of defects. Assuming the boundary condition for s is a positive constant well away from zero, if κ is large, then $\int_\Omega \kappa|\nabla s|^2 dx$ dominates the energy and s stays close to a positive constant within the domain Ω. Thus, defects are less likely to occur. If κ is small (say $\kappa < 1$), then $\int_\Omega s^2|\nabla\mathbf{n}|^2 dx$ dominates the energy, and s may vanish in regions of Ω and induce a defect. This was confirmed by our numerical experiments in [61,62]. The physically relevant case $0 < \kappa < 1$ is the more difficult case with regard to proving Γ-convergence (see [61]) because the energy is no longer convex.

2.2. Discretization of the energy

Let $\mathcal{T}_h = \{T\}$ be a conforming simplicial triangulation of Ω. The set of nodes (vertices) of $\mathcal{T}_h$ is denoted $\mathcal{N}_h$ and has cardinality n. We demand that $\mathcal{T}_h$ be *weakly acute*, namely

$$k_{ij} := -\int_\Omega \nabla\phi_i \cdot \nabla\phi_j \, dx \geq 0 \quad \text{for all } i \neq j, \tag{8}$$

where ϕ_i is the standard "hat" basis function associated with node $x_i \in \mathcal{N}_h$. We indicate with $\omega_i = \text{supp } \phi_i$ the patch of a node x_i (i.e. the "star" of elements in $\mathcal{T}_h$ that contain the vertex x_i). Of course, (8) imposes a severe geometric restriction on $\mathcal{T}_h$ [71,72] (especially in three dimensions). We recall the following characterization of (8) for $d = 2$.

Lemma 1 (*Weak acuteness in two dimensions*). *For any pair of triangles T_1, T_2 in $\mathcal{T}_h$ in two space dimensions that share a common edge e, let α_i be the angle in T_i opposite to e (for $i = 1, 2$). Then* (8) *holds if and only if $\alpha_1 + \alpha_2 \leq 180°$ for every edge e.*

Generalizations of Lemma 1 to three dimensions, involving interior dihedral angles of tetrahedra, can be found in [73,74]. Note that a *non-obtuse* mesh (one where *all* interior angles are bounded by $90°$) is automatically weakly-acute.

The method uses the following finite element spaces:

$$\mathbb{S}_h := \{s_h \in H^1(\Omega) : s_h|_T \text{ is affine for all } T \in \mathcal{T}_h\},$$

$$\mathbb{U}_h := \{\mathbf{u}_h \in [H^1(\Omega)]^d : \mathbf{u}_h|_T \text{ is affine in each component for all } T \in \mathcal{T}_h\}, \tag{9}$$

$$\mathbb{N}_h := \{\mathbf{n}_h \in \mathbb{U}_h : |\mathbf{n}_h(x_i)| = 1 \text{ for all nodes } x_i \in \mathcal{N}_h\},$$

where $\mathbb{N}_h$ imposes the unit length constraint *at the vertices* of the mesh.

Let I_h denote the piecewise linear Lagrange interpolation operator on mesh $\mathcal{T}_h$ with values in either $\mathbb{S}_h$ or $\mathbb{U}_h$. We have the following *discrete* version of the admissible class:

$$\mathbb{A}_h := \{(s_h, \mathbf{u}_h) \in \mathbb{S}_h \times \mathbb{U}_h : -1/2 < s_h < 1 \text{ in } \Omega, \ \mathbf{u}_h = I_h[s_h \mathbf{n}_h] \text{ where } \mathbf{n}_h \in \mathbb{N}_h\}. \tag{10}$$

Next, we let $g_h := I_h g$ and $\mathbf{r}_h := I_h \mathbf{r}$ be the discrete Dirichlet data, and introduce the discrete spaces that include (Dirichlet) boundary conditions

$$\mathbb{S}_h(\Gamma_s, g_h) := \{s_h \in \mathbb{S}_h : s_h|_{\Gamma_s} = g_h\}, \quad \mathbb{U}_h(\Gamma_{\mathbf{u}}, \mathbf{r}_h) := \{\mathbf{u}_h \in \mathbb{U}_h : \mathbf{u}_h|_{\Gamma_{\mathbf{u}}} = \mathbf{r}_h\},$$

as well as the discrete admissible class with boundary conditions:

$$\mathbb{A}_h(g_h, \mathbf{r}_h) := \{(s_h, \mathbf{u}_h) \in \mathbb{A}_h : s_h \in \mathbb{S}_h(\Gamma_s, g_h), \mathbf{u}_h \in \mathbb{U}_h(\Gamma_{\mathbf{u}}, \mathbf{r}_h)\}. \tag{11}$$

In view of (6), we can also impose the Dirichlet condition $\mathbf{n}_h = I_h[g_h^{-1}\mathbf{r}_h]$ on $\partial\Omega$.

Our discrete version of $E_1[s, \mathbf{n}]$ is "derived" by invoking basic properties of the stiffness matrix entries k_{ij}. First note $\sum_{j=1}^n k_{ij} = 0$ for all $x_i \in \mathcal{N}_h$, and for piecewise linear $s_h = \sum_{i=1}^n s_h(x_i)\phi_i$ we have

$$\int_\Omega |\nabla s_h|^2 dx = -\sum_{i=1}^n k_{ii} s_h(x_i)^2 - \sum_{i,j=1,i\neq j}^n k_{ij} s_h(x_i) s_h(x_j).$$

Thus, using $k_{ii} = -\sum_{j\neq i} k_{ij}$ and the symmetry $k_{ij} = k_{ji}$, we get

$$\int_\Omega |\nabla s_h|^2 dx = \sum_{i,j=1}^n k_{ij} s_h(x_i)\big(s_h(x_i) - s_h(x_j)\big)$$

$$= \frac{1}{2}\sum_{i,j=1}^n k_{ij}\big(s_h(x_i) - s_h(x_j)\big)^2 = \frac{1}{2}\sum_{i,j=1}^n k_{ij}\big(\delta_{ij}s_h\big)^2, \tag{12}$$

where we define

$$\delta_{ij}s_h := s_h(x_i) - s_h(x_j), \quad \delta_{ij}\mathbf{n}_h := \mathbf{n}_h(x_i) - \mathbf{n}_h(x_j). \tag{13}$$

Therefore, we define the discrete energy to be

$$E_1^h[s_h, \mathbf{n}_h] := \frac{\kappa}{2}\sum_{i,j=1}^n k_{ij}\big(\delta_{ij}s_h\big)^2 + \frac{1}{2}\sum_{i,j=1}^n k_{ij}\left(\frac{s_h(x_i)^2 + s_h(x_j)^2}{2}\right)|\delta_{ij}\mathbf{n}_h|^2, \tag{14}$$

where the second term is a first order approximation of $\int_\Omega s^2|\nabla\mathbf{n}|^2$, which is novel in the finite element literature [61]. The double well energy is discretized in the usual way:

$$E_2^h[s_h] := \int_\Omega \psi(s_h(x))dx. \tag{15}$$

The specific form of (14) lies on the fact that it makes the nodal values of s_h and $\mathbf{n}_h$ *readily accessible* for analysis. The identity in (3) is obtained (at the continuous level) by taking advantage of the unit length constraint $|\mathbf{n}| = 1$. However, at the discrete level, we only impose the unit length constraint at the *nodes* of the mesh, and we cannot hope for much more because $\mathbf{n}_h$ is a piecewise polynomial. Hence, in order to obtain a similar identity to (3) (see Lemma 2 below), we need access to nodal values. In [61], we show that the discrete energy (14) allows us to handle the degenerate coefficient s_h^2 *without* regularization.

The discrete formulation is as follows. Find $(s_h, \mathbf{n}_h) \in \mathbb{S}_h(\Gamma_s, g_h) \times \mathbb{N}_h(\Gamma_\mathbf{n}, \mathbf{r}_h)$ such that the following energy is minimized:

$$E^h[s_h, \mathbf{n}_h] := E_1^h[s_h, \mathbf{n}_h] + E_2^h[s_h]. \tag{16}$$

3. Review of the method

3.1. Energy inequality

Our discrete energy (14) satisfies a discrete version of (3) [35,39], which is a key component of our analysis in [61]. To see this, we introduce $\widetilde{s}_h := I_h|s_h|$ and two discrete versions of the vector field $\mathbf{u}$

$$\mathbf{u}_h := I_h[s_h \mathbf{n}_h] \in \mathbb{U}_h, \quad \widetilde{\mathbf{u}}_h := I_h[\widetilde{s}_h \mathbf{n}_h] \in \mathbb{U}_h. \tag{17}$$

Note that both $(s_h, \mathbf{u}_h)$, $(\widetilde{s}_h, \widetilde{\mathbf{u}}_h)$ are in $\mathbb{A}_h(g_h, \mathbf{r}_h)$. We now state a discrete version of (3).

Lemma 2 *(Discrete energy inequality). Let the mesh $\mathcal{T}_h$ satisfy (8). If $(s_h, \mathbf{u}_h) \in \mathbb{A}_h(g_h, \mathbf{r}_h)$, then, for any $\kappa > 0$, the discrete energy (14) satisfies*

$$E_1^h[s_h, \mathbf{n}_h] \geq (\kappa - 1) \int\limits_\Omega |\nabla s_h|^2 dx + \int\limits_\Omega |\nabla \mathbf{u}_h|^2 dx =: \widetilde{E}_1^h[s_h, \mathbf{u}_h], \tag{18}$$

as well as

$$E_1^h[s_h, \mathbf{n}_h] \geq (\kappa - 1) \int\limits_\Omega |\nabla \widetilde{s}_h|^2 dx + \int\limits_\Omega |\nabla \widetilde{\mathbf{u}}_h|^2 dx =: \widetilde{E}_1^h[\widetilde{s}_h, \widetilde{\mathbf{u}}_h]. \tag{19}$$

In fact, the following inequalities are valid [61]

$$E_1^h[s_h, \mathbf{n}_h] - \widetilde{E}_1^h[s_h, \mathbf{u}_h] \geq \mathcal{E}_h, \qquad E_1^h[s_h, \mathbf{n}_h] - \widetilde{E}_1^h[\widetilde{s}_h, \widetilde{\mathbf{u}}_h] \geq \widetilde{\mathcal{E}}_h, \tag{20}$$

where

$$\mathcal{E}_h := \frac{1}{4} \sum_{i,j=1}^n k_{ij} (\delta_{ij} s_h)^2 |\delta_{ij} \mathbf{n}_h|^2, \qquad \widetilde{\mathcal{E}}_h := \frac{1}{4} \sum_{i,j=1}^n k_{ij} (\delta_{ij} \widetilde{s}_h)^2 |\delta_{ij} \mathbf{n}_h|^2. \tag{21}$$

Note that $\mathcal{E}_h, \widetilde{\mathcal{E}}_h \geq 0$ because $k_{ij} \geq 0$ for $i \neq j$. We refer to [61] for further details.

3.2. Minimization scheme

We summarize the discrete quasi-gradient flow scheme in [61] which we use to compute discrete minimizers.

3.2.1. Boundary conditions
In the continuous setting, Dirichlet boundary conditions are enforced in the space. Let

$$H_\Gamma^1(\Omega) := \{v \in H^1(\Omega) : v = 0 \text{ on } \Gamma\}, \tag{22}$$

where $\Gamma \subset \partial\Omega$ is either Γ_s, $\Gamma_\mathbf{n}$, and $s \in g + H_{\Gamma_s}^1(\Omega)$, $\mathbf{u} \in \mathbf{r} + [H_{\Gamma_\mathbf{u}}^1(\Omega)]^d$. We assume $\Gamma_\mathbf{n} = \Gamma_\mathbf{u} \subset \Gamma_s$ and (6) to be valid on Γ_s. The trace $\mathbf{n} = \mathbf{q} := g^{-1}\mathbf{r}$ is thus well defined on $\Gamma_\mathbf{n}$.

The superscript k will stand for an iteration counter. Therefore, $s_h^k \in \mathbb{S}_h(\Gamma, g_h)$ and $\mathbf{n}_h^k \in \mathbb{N}_h(\Gamma_\mathbf{n}, \mathbf{q}_h)$ indicate iterates satisfying Dirichlet boundary conditions where $g_h := I_h g$ and $\mathbf{q}_h := I_h\mathbf{q}$. We will further simplify the notation in some places upon writing:

$$s_i^k := s_h^k(x_i), \quad \mathbf{n}_i^k := \mathbf{n}_h^k(x_i), \quad z_i := z_h(x_i), \quad \mathbf{v}_i := \mathbf{v}_h(x_i).$$

3.2.2. First order variation
We start with the energy E_1^h. Due to the unit length constraint at the nodes in $\mathbb{N}_h$ (see (9)), we introduce the space of discrete tangential variations:

$$\mathbb{U}_h^\perp(\mathbf{n}_h) = \{\mathbf{v}_h \in \mathbb{U}_h : \mathbf{v}_h(x_i) \cdot \mathbf{n}_h(x_i) = 0 \text{ for all nodes } x_i \in \mathcal{N}_h\}. \tag{23}$$

Next, the first order variation of $E_1^h[s_h^k, \mathbf{n}_h^k]$ in the direction $\mathbf{v}_h \in \mathbb{U}_h^\perp(\mathbf{n}_h^k) \cap H_{\Gamma_\mathbf{n}}^1(\Omega)$ reads

$$\delta_{\mathbf{n}_h} E_1^h[s_h^k, \mathbf{n}_h^k; \mathbf{v}_h] = \sum_{i,j=1}^n k_{ij} \left(\frac{(s_i^k)^2 + (s_j^k)^2}{2} \right) (\delta_{ij} \mathbf{n}_h^k) \cdot (\delta_{ij} \mathbf{v}_h). \tag{24}$$

The first order variation of $E_1^h[s_h^k, \mathbf{n}_h^k]$ in the direction $z_h \in \mathbb{S}_h \cap H^1_{\Gamma_s}(\Omega)$ consists of two terms

$$\delta_{s_h} E_1^h[s_h^k, \mathbf{n}_h^k; z_h] = \kappa \sum_{i,j=1}^n k_{ij} \left(\delta_{ij} s_h^k \right) \left(\delta_{ij} z_h \right) + \sum_{i,j=1}^n k_{ij} |\delta_{ij} \mathbf{n}_h^k|^2 \left(\frac{s_i^k z_i + s_j^k z_j}{2} \right). \tag{25}$$

We next consider the energy E_2^h. In order to guarantee a monotonically energy decreasing scheme, we employ the convex splitting technique in [75–77], i.e. we split the double well potential ψ into a convex and concave part. Let ψ_c and ψ_e be both convex for all $s \in (-1/2, 1)$ so that $\psi(s) = \psi_c(s) - \psi_e(s)$, and set

$$\delta_{s_h} E_2^h[s_h^{k+1}; z_h] := \int_{\Omega} \left[\psi_c'(s_h^{k+1}) - \psi_e'(s_h^k) \right] z_h dx, \tag{26}$$

which yields the inequality

$$\int_{\Omega} \psi(s_h^{k+1}) dx - \int_{\Omega} \psi(s_h^k) dx \le \delta_{s_h} E_2^h[s_h^{k+1}; s_h^{k+1} - s_h^k], \tag{27}$$

for any s_h^k and s_h^{k+1} in $\mathbb{S}_h$ [61]. Note that

$$\delta_{\mathbf{n}_h} E^h[s_h^k, \mathbf{n}_h^k; \mathbf{v}_h] = \delta_{\mathbf{n}_h} E_1^h[s_h^k, \mathbf{n}_h^k; \mathbf{v}_h],$$
$$\delta_{s_h} E^h[s_h^k, \mathbf{n}_h^k; z_h] = \delta_{s_h} E_1^h[s_h^k, \mathbf{n}_h^k; z_h] + \delta_{s_h} E_2^h[s_h^k, \mathbf{n}_h^k; z_h].$$

3.2.3. Discrete quasi-gradient flow algorithm

Our scheme for minimizing $E^h[s_h, \mathbf{n}_h]$, defined in (16), is an alternating direction method, which minimizes with respect to $\mathbf{n}_h$ and evolves s_h separately in the steepest descent direction during each iteration. Therefore, this algorithm is not a standard gradient flow but rather a quasi-gradient flow.

Algorithm: Given $(s_h^0, \mathbf{n}_h^0)$ in $\mathbb{S}_h(\Gamma_s, g_h) \times \mathbb{N}_h(\Gamma_\mathbf{n}, \mathbf{q}_h)$, iterate Steps (a)–(c) for $k \ge 0$.

Step (a): Minimization. Find $\mathbf{t}_h^k \in \mathbb{U}_h^\perp(\mathbf{n}_h^k) \cap H^1_{\Gamma_\mathbf{n}}(\Omega)$ such that $\mathbf{n}_h^k + \mathbf{t}_h^k$ minimizes the energy $E^h[s_h^k, \mathbf{n}_h^k + \mathbf{v}_h]$ for all $\mathbf{v}_h$ in $\mathbb{U}_h^\perp(\mathbf{n}_h^k) \cap H^1_{\Gamma_\mathbf{n}}(\Omega)$, i.e. $\mathbf{t}_h^k$ satisfies

$$\delta_{\mathbf{n}_h} E^h[s_h^k, \mathbf{n}_h^k + \mathbf{t}_h^k; \mathbf{v}_h] = 0, \quad \forall \mathbf{v}_h \in \mathbb{U}_h^\perp(\mathbf{n}_h^k) \cap H^1_{\Gamma_\mathbf{n}}(\Omega).$$

Step (b): Projection. Normalize $\mathbf{n}_i^{k+1} := \frac{\mathbf{n}_i^k + \mathbf{t}_i^k}{|\mathbf{n}_i^k + \mathbf{t}_i^k|}$ at all nodes $x_i \in \mathcal{N}_h$.

Step (c): Gradient flow. Using $(s_h^k, \mathbf{n}_h^{k+1})$, find s_h^{k+1} in $\mathbb{S}_h(\Gamma_s, g_h)$ such that

$$\int_{\Omega} \frac{s_h^{k+1} - s_h^k}{\delta t} z_h = -\delta_{s_h} E^h[s_h^{k+1}, \mathbf{n}_h^{k+1}; z_h], \quad \forall z_h \in \mathbb{S}_h \cap H^1_{\Gamma_s}(\Omega).$$

In the numerical experiments, we impose Dirichlet boundary conditions for both s_h^k and $\mathbf{n}_h^k$ on subsets of the boundary. Note that the scheme has no restriction on the time step thanks to the implicit Euler method in Step (c).

The quasi-gradient flow scheme has a monotone energy decreasing property, provided the mesh $\mathcal{T}_h$ is weakly acute (8) [71,72].

Theorem 3 (Monotonicity [61]). *Let $\mathcal{T}_h$ satisfy (8). The iterate $(s_h^{k+1}, \mathbf{n}_h^{k+1})$ of the Algorithm (discrete quasi-gradient flow) of Section 3.2.3 exists and satisfies*

$$E^h[s_h^{k+1}, \mathbf{n}_h^{k+1}] \le E^h[s_h^k, \mathbf{n}_h^k] - \frac{1}{\delta t} \int_{\Omega} (s_h^{k+1} - s_h^k)^2 dx.$$

Equality holds if and only if $(s_h^{k+1}, \mathbf{n}_h^{k+1}) = (s_h^k, \mathbf{n}_h^k)$ (equilibrium state).

We extend this result in Theorem 8 to include additional energy terms; see (101).

4. Implementation

We implemented our method using the MATLAB/C++ finite element toolbox FELICITY [78]. In this section, we give details on forming the ensuing discrete systems, and how to solve part (a) of the quasi-gradient flow algorithm in 3-D using the tangent space. For all 3-D simulations, we used the algebraic multi-grid solver (AGMG) [79–82] to solve the linear systems in parts (a) and (c) of the quasi-gradient flow algorithm. In 2-D, we simply used the "backslash" command in MATLAB.

4.1. Finite element matrices

Implementing the algorithm requires construction of the discrete energy, as well as its variational derivative. This requires the symmetric mass and stiffness finite element matrices: $M := (m_{ij})_{i,j=1}^n$, $K := (-k_{ij})_{i,j=1}^n$, where

$$m_{ij} = \int_\Omega \phi_i \phi_j, \quad k_{ij} = -\int_\Omega \nabla\phi_i \cdot \nabla\phi_j, \tag{28}$$

and $\{\phi_i\}_{i=1}^n$ is the set of basis functions of the space $\mathbb{S}_h$.

4.2. Finite element functions and coefficient vectors

The function s_h is represented by a linear combination of $\{\phi_i\}_{i=1}^n$. If the dimension of Ω is d, then the vector field $\mathbf{n}_h$ has d components, where each component is written as a linear combination of $\{\phi_i\}_{i=1}^n$. The nodal values of s_h and $\mathbf{n}_h$, at node x_i, are denoted by s_i and $\mathbf{n}_i$.

The corresponding coefficient vectors (arrays) are denoted with non-italicized capital letters, i.e. $S \in \mathbb{R}^n$, $N \in \mathbb{R}^{dn}$, such that

$$S = [S_1, S_2, ..., S_n]^T, \quad N = [N_1, N_2, ..., N_n, N_{n+1}, ...N_{dn}]^T, \tag{29}$$

where $S_i := s_i$ and

$$\begin{aligned} N_i &= \mathbf{n}_i \cdot \mathbf{e}_1, \\ N_{i+n} &= \mathbf{n}_i \cdot \mathbf{e}_2, \\ N_{i+2n} &= \mathbf{n}_i \cdot \mathbf{e}_3, \\ &\vdots \\ N_{i+(k-1)n} &= \mathbf{n}_i \cdot \mathbf{e}_k, \\ &\vdots \\ N_{i+(d-1)n} &= \mathbf{n}_i \cdot \mathbf{e}_d, \end{aligned} \tag{30}$$

for $1 \leq i \leq n$, where $\{\mathbf{e}_i\}_{i=1}^d$ are the canonical basis vectors of $\mathbb{R}^d$. In other words, we store the coefficients of $\mathbf{n}_h$ so that the $\mathbf{e}_1$ components are first, followed by the $\mathbf{e}_2$ components, and so on. Therefore,

$$\mathbf{n}_h(x_i) \equiv \mathbf{n}_i = (N_i, N_{i+n}, N_{i+2n}, ..., N_{i+(d-1)n})^T, \quad \text{for all } 1 \leq i \leq n.$$

4.3. Discrete variations

Let us write $\delta_{s_h} E_1^h[\Omega, s_h, \mathbf{n}_h; z_h]$ from (25) in a different form:

$$\delta_{s_h} E_1^h[s_h, \mathbf{n}_h; z_h] = 2\kappa Z^T K S + \frac{1}{2} \sum_{i,j=1}^n (A(\mathbf{n}_h))_{ij} (S_i Z_i + S_j Z_j), \tag{31}$$

where $Z \in \mathbb{R}^n$ is the coefficient vector corresponding to $z_h \in \mathbb{S}_h$, and $A(\mathbf{n}_h) \equiv (A(\mathbf{n}_h))_{i,j=1}^n$ is the symmetric matrix defined by

$$(A(\mathbf{n}_h))_{ij} = k_{ij} \sum_{r=1}^d (N_{i+(r-1)n} - N_{j+(r-1)n})^2. \tag{32}$$

Lemma 4. *Let A be an arbitrary $n \times n$ matrix, and Y, Z be arbitrary $n \times 1$ column vectors. Then*

$$\sum_{i,j=1}^{n} (A)_{ij} Y_i Z_i = \sum_{i=1}^{n} Y_i Z_i \underbrace{\sum_{j=1}^{n} (A)_{ij}}_{=:(\widehat{A})_i} = Z^T [\text{diag}(\widehat{A})] Y, \tag{33}$$

where $\widehat{A}$ is a $n \times 1$ column vector and $[\text{diag}(\widehat{A})]$ is a $n \times n$ diagonal matrix formed from $\{(\widehat{A})_1, (\widehat{A})_2, ..., (\widehat{A})_n\}$.

Continuing with (31), and using (33), we get

$$\delta_{s_h} E_1^h[s_h, \mathbf{n}_h; z_h] = 2\kappa Z^T K S + \frac{1}{2} \sum_{i,j=1}^{n} (A(\mathbf{n}_h))_{ij} S_i Z_i + \frac{1}{2} \sum_{i,j=1}^{n} (A(\mathbf{n}_h))_{ij} S_j Z_j,$$
$$= 2\kappa Z^T K S + Z^T D(\mathbf{n}_h) S, \tag{34}$$

where

$$D(\mathbf{n}_h) = \text{diag}(\widehat{A(\mathbf{n}_h)}), \quad (\widehat{A(\mathbf{n}_h)})_i = \sum_{j=1}^{n} (A(\mathbf{n}_h))_{ij}.$$

Next, we write out $\delta_{\mathbf{n}_h} E_1^h[s_h, \mathbf{n}_h; \mathbf{v}_h]$ from (24) in a different form:

$$\delta_{\mathbf{n}_h} E_1^h[s_h, \mathbf{n}_h; \mathbf{v}_h] = \sum_{r=1}^{d} \underbrace{\sum_{i,j=1}^{n} k_{ij} \left(\frac{S_i^2 + S_j^2}{2} \right) \Theta_{ij}(r)}_{\Xi_r :=}, \tag{35}$$

where we defined

$$\Theta_{ij}(r) := \left(N_{i+(r-1)n} - N_{j+(r-1)n} \right) \cdot \left(V_{i+(r-1)n} - V_{j+(r-1)n} \right), \tag{36}$$

with $V \in \mathbb{R}^{dn}$ the coefficient vector corresponding to $\mathbf{v}_h \in \mathbb{U}_h$.

Let us now focus on Ξ_1:

$$\Xi_1 = \sum_{i,j=1}^{n} k_{ij} \left(\frac{S_i^2 + S_j^2}{2} \right) (N_i - N_j) \cdot (V_i - V_j),$$
$$= \frac{1}{2} \sum_{i,j=1}^{n} (\widetilde{\mathbf{A}}(s_h))_{ij} (N_i \cdot V_i - N_i \cdot V_j - N_j \cdot V_i + N_j \cdot V_j), \tag{37}$$

where $\widetilde{\mathbf{A}}(s_h)$ is the $n \times n$ symmetric matrix defined by

$$\widetilde{\mathbf{A}}(s_h) \equiv ((\widetilde{\mathbf{A}}(s_h))_{ij})_{i,j=1}^{n}, \quad (\widetilde{\mathbf{A}}(s_h))_{ij} = k_{ij} \left(S_i^2 + S_j^2 \right). \tag{38}$$

Using symmetry gives

$$\Xi_1 = \frac{1}{2} \sum_{i,j=1}^{n} 2(\widetilde{\mathbf{A}}(s_h))_{ij} (N_i \cdot V_i - N_j \cdot V_i)$$
$$= \sum_{i,j=1}^{n} (\widetilde{\mathbf{A}}(s_h))_{ij} (N_i \cdot V_i) - \sum_{i,j=1}^{n} (\widetilde{\mathbf{A}}(s_h))_{ij} (N_j \cdot V_i) \tag{39}$$
$$= V(1:n)^T \widetilde{\mathbf{D}}(s_h) N(1:n) - V(1:n)^T \widetilde{\mathbf{A}}(s_h) N(1:n),$$

where $V(1:n)$ denotes the first n components of V, etc., and

$$\widetilde{\mathbf{D}}(s_h) = \text{diag}(\widehat{\widetilde{\mathbf{A}}(s_h)}), \quad (\widehat{\widetilde{\mathbf{A}}(s_h)})_i = \sum_{j=1}^{n} (\widetilde{\mathbf{A}}(s_h))_{ij}. \tag{40}$$

Applying the same argument to Ξ_r, we get

$$\Xi_r = V((r-1)n+1:rn)^T \widetilde{\mathbf{D}}(s_h) N((r-1)n+1:rn)$$
$$- V((r-1)n+1:rn)^T \widetilde{\mathbf{A}}(s_h) N((r-1)n+1:rn). \tag{41}$$

Therefore, recalling (35), we obtain

$$\delta_{\mathbf{n}_h} E_1^h[s_h, \mathbf{n}_h; \mathbf{v}_h] = V^T \mathbf{D}(s_h) N - V^T \mathbf{A}(s_h) N, \tag{42}$$

where $\mathbf{D}(s_h)$ is $dn \times dn$ block diagonal (with d identical blocks), where each block equals $\widetilde{\mathbf{D}}(s_h)$ defined in (40); similarly, $\mathbf{A}(s_h)$ is $dn \times dn$ block diagonal (with d identical blocks), where each block equals $\widetilde{\mathbf{A}}(s_h)$ defined in (38).

4.4. Discrete quasi-gradient flow

Given $(s_h^k, \mathbf{n}_h^k)$, we have the corresponding coefficient vectors (S^k, N^k). We now rewrite the Algorithm in Section 3.2.3 in terms of the matrices and vectors introduced earlier.

Step (a): By (42), we solve the following linear system *in the tangent space* (see Section 4.5) to obtain $\mathbf{t}_h^k$:

$$\left[\mathbf{D}(s_h^k) - \mathbf{A}(s_h^k)\right] T^k = -\left[\mathbf{D}(s_h^k) - \mathbf{A}(s_h^k)\right] N^k, \tag{43}$$

where T^k in $\mathbb{R}^{dn}$ is the coefficient vector corresponding to $\mathbf{t}_h^k$ in $\mathbb{U}_h^\perp(\mathbf{n}_h^k) \cap H^1_{\Gamma_\mathbf{n}}(\Omega)$. Note that (43) must be modified to enforce Dirichlet boundary conditions (if necessary).

Remark 5 *(Solving a degenerate system).* The system matrix in (43) is symmetric positive semi-definite, which is easily verified from the properties of $\mathbf{D}(s_h^k)$. Moreover, it is positive definite if $|s_h^k| > 0$ everywhere. Hence, the system can be solved by any method for symmetric positive definite matrices.

When $s_h^k = 0$ at a sufficient number of nodes, the matrix will be singular. In this case, one could use a conjugate gradient method [83]; note that the right-hand-side of (43) is guaranteed to be in the column space of the system matrix.

In 3-D, we solve (43) using AGMG [79–82], which has the following condition: all the diagonal entries of the matrix must be positive. If this is not the case, we must modify the system matrix in (43) accordingly. This is most easily done by using the minimizing movement strategy described in Section 7.1, which effectively adds an identity matrix (with small weight $\rho > 0$) to the system matrix in (43).

Step (b): Apply the normalization step at all nodes to obtain $\mathbf{n}_h^{k+1}$, i.e.

(1): $W := N^k + T^k$,

(2): $\alpha_i := \left(W_i^2 + W_{i+n}^2 + \cdots + W_{i+(d-1)n}^2\right)^{1/2}$, for all $1 \le i \le n$,

(3): $N_{i+(r-1)n}^{k+1} := W_{i+(r-1)n}/\alpha_i$, for all $1 \le i \le n$, and $r = 1, 2, ..., d$,

where N^{k+1} is the coefficient vector corresponding to $\mathbf{n}_h^{k+1}$.

Step (c): Use the following convex splitting of the double well: $\psi(s) = \psi_c(s) - \psi_e(s)$, where we choose

$$\psi_c(s) = c_0 s^2, \qquad \psi_e(s) = c_0 s^2 - \psi(s),$$

and select $c_0 > 0$ large enough to ensure that $\psi_c(s), \psi_e(s)$ are convex for all $-1/2 < s < 1$. Recall (26) and note that $\psi_c'(s)$ is linear. Hence, we can write

$$\delta_{s_h} E_2^h[s_h^{k+1}; z_h] = \int_\Omega [\psi_c'(s_h^{k+1}) - \psi_e'(s_h^k)] z_h dx$$
$$= 2c_0 Z^T M S^{k+1} - Z^T B(s_h^k),$$

where Z is the coefficient vector corresponding to z_h in $\mathbb{S}_h \cap H^1_{\Gamma_s}(\Omega)$, and $B(s_h^k) = (B_1, ..., B_n)^T$ in $\mathbb{R}^n$ is a column vector defined by

$$B_i = \int_\Omega \psi_e'(s_h^k)\phi_i dx, \quad \text{for all } 1 \le i \le n. \tag{44}$$

Therefore, using (34), we solve the following linear system for S^{k+1}:

$$\left[M + 2\delta t \kappa K + \delta t D(\mathbf{n}_h^{k+1}) + 2c_0 \delta t M\right] S^{k+1} = M S^k + \delta t B(s_h^k), \tag{45}$$

where S^{k+1} is the coefficient vector corresponding to s_h^{k+1}. Note that (45) must be modified to enforce Dirichlet boundary conditions.

4.5. Tangential variations

Solving Step (a) of the Algorithm requires a tangential basis for the test function and the solution. However, forming the matrix system is easily done by *first ignoring* the tangential variation constraint (i.e. arbitrary variations), followed by a simple modification of the matrix system. For a concrete realization of the procedure, we consider the case $d = 3$.

Let $AT^k = C$ represent the linear system in Step (a) (ignoring the tangent space constraint), where A is a $dn \times dn$ matrix, and T^k, C are column vectors in $\mathbb{R}^{dn}$. Note that the solution vector T^k is the coefficient vector associated with the finite element function $\mathbf{t}_h^k$ in $\mathbb{U}_h^\perp(\mathbf{n}_h^k)$ (recall Section 3.2.3).

Multiplying the linear system by a column vector V in $\mathbb{R}^{dn}$, we seek to find T^k in $\mathbb{R}^{dn}$ such that

$$V^T A T^k = V^T C, \quad \text{for all } V \in \mathbb{R}^{dn}. \tag{46}$$

Next, using $\mathbf{n}_h^k$ in $\mathbb{N}_h$, find $\mathbf{q}_h^k$, $\mathbf{w}_h^k$ in $\mathbb{U}_h^\perp(\mathbf{n}_h^k)$ such that $\{\mathbf{n}_h^k(x_i), \mathbf{q}_h^k(x_i), \mathbf{w}_h^k(x_i)\}$ forms an orthonormal basis of $\mathbb{R}^3$ at each node x_i, i.e. find an orthonormal basis of $\mathbb{U}_h$. Let Q^k, W^k in $\mathbb{R}^{dn}$ be the coefficient vectors associated with $\mathbf{q}_h^k$, $\mathbf{w}_h^k$.

Since $\mathbf{t}_h^k$ is in the tangent space, we can expand T^k as

$$T_{i+(r-1)n}^k = F_i Q_{i+(r-1)n}^k + G_i W_{i+(r-1)n}^k, \quad \text{for all } 1 \le i \le n, 1 \le r \le 3, \tag{47}$$

where $F = (F_1, ..., F_n)^T$, $G = (G_1, ..., G_n)^T$ are unknown solution (column) vectors in $\mathbb{R}^n$. With this, we can write the expansion of T^k as

$$T^k = \begin{bmatrix} D_1(Q^k) \\ D_2(Q^k) \\ D_3(Q^k) \end{bmatrix} F + \begin{bmatrix} D_1(W^k) \\ D_2(W^k) \\ D_3(W^k) \end{bmatrix} G, \tag{48}$$

where $D_1(\cdot)$, $D_2(\cdot)$, $D_3(\cdot)$ are $n \times n$ diagonal matrices defined by

$$\begin{aligned} D_r(Q^k) &:= \text{diag}[Q^k((r-1)n + 1 : rn)], \ \text{for } r = 1, 2, 3, \\ D_r(W^k) &:= \text{diag}[W^k((r-1)n + 1 : rn)], \ \text{for } r = 1, 2, 3. \end{aligned} \tag{49}$$

Furthermore, we make a similar tangential expansion for V:

$$V = \begin{bmatrix} D_1(Q^k) \\ D_2(Q^k) \\ D_3(Q^k) \end{bmatrix} Y + \begin{bmatrix} D_1(W^k) \\ D_2(W^k) \\ D_3(W^k) \end{bmatrix} Z, \tag{50}$$

where $Y = (Y_1, ..., Y_n)^T$, $Z = (Z_1, ..., Z_n)^T$ are arbitrary column vectors in $\mathbb{R}^n$.

Now note that A is symmetric block diagonal with d *identical* blocks $\widetilde{A}$ (recall (42)). And the orthogonality of $\mathbf{q}_h^k$ and $\mathbf{w}_h^k$ at the nodes is equivalent to

$$Q_i^k W_i^k + Q_{n+i}^k W_{n+i}^k + Q_{2n+i}^k W_{2n+i}^k = \sum_{r=1}^3 Q_{(r-1)n+i}^k W_{(r-1)n+j}^k = 0, \tag{51}$$

for all $1 \le i \le n$. From this, one can show that

$$\begin{bmatrix} D_1(Q^k) & D_2(Q^k) & D_3(Q^k) \end{bmatrix} A \begin{bmatrix} D_1(W^k) \\ D_2(W^k) \\ D_3(W^k) \end{bmatrix} = \sum_{r=1}^3 D_r(Q^k)\widetilde{A} D_r(W^k) = 0 \in \mathbb{R}^{n \times n}. \tag{52}$$

Indeed, looking at the (i, j) entry and using (49), we have

$$\begin{aligned} \sum_{r=1}^3 [D_r(Q^k)\widetilde{A} D_r(W^k)]_{ij} &= \sum_{r=1}^3 Q_{(r-1)n+i}^k (\widetilde{A})_{ij} W_{(r-1)n+j}^k \\ &= (\widetilde{A})_{ij} \sum_{r=1}^3 Q_{(r-1)n+i}^k W_{(r-1)n+j}^k = 0, \end{aligned}$$

by (51).

Therefore, plugging the expansions (48), (50) into (46), accounting for (52), and using the arbitrariness of Y, Z, we obtain two decoupled, $n \times n$ linear systems to solve:

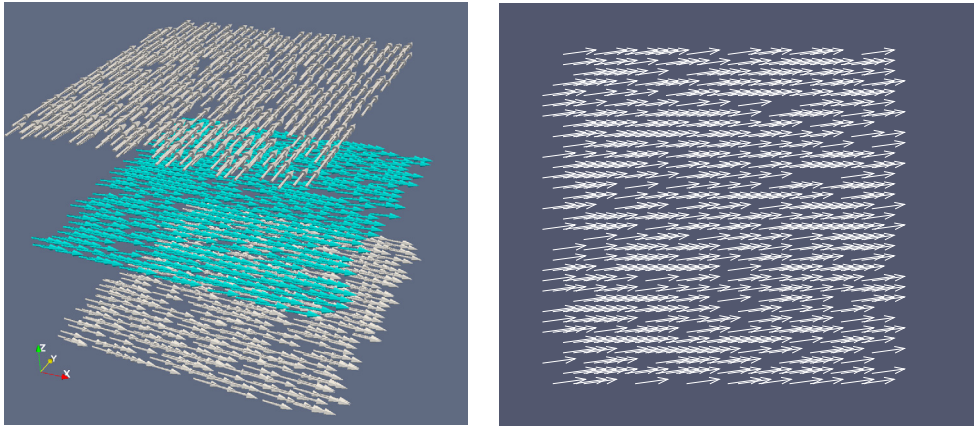$$A(Q^k)F = C(Q^k), \qquad A(W^k)G = C(W^k), \tag{53}$$

Fig. 3. Simulation results for Section 4.6. The director field is shown on the planes $z = 0.1, 0.5, 0.9$, which indicates that it is piecewise constant (see (55)). On the right, the $z = 0.5$ plane case indicates that the director field takes on an intermediate value between $(1, 0, 0)^T$ and $(0, 1, 0)^T$. The numerical solution was computed at mesh level $\ell = 5$.

which are defined by

$$A(\mathsf{Q}^k) = \begin{bmatrix} D_1(\mathsf{Q}^k) & D_2(\mathsf{Q}^k) & D_3(\mathsf{Q}^k) \end{bmatrix} A \begin{bmatrix} D_1(\mathsf{Q}^k) \\ D_2(\mathsf{Q}^k) \\ D_3(\mathsf{Q}^k) \end{bmatrix},$$

$$A(\mathsf{W}^k) = \begin{bmatrix} D_1(\mathsf{W}^k) & D_2(\mathsf{W}^k) & D_3(\mathsf{W}^k) \end{bmatrix} A \begin{bmatrix} D_1(\mathsf{W}^k) \\ D_2(\mathsf{W}^k) \\ D_3(\mathsf{W}^k) \end{bmatrix},$$

$$C(\mathsf{Q}^k) = \begin{bmatrix} D_1(\mathsf{Q}^k) & D_2(\mathsf{Q}^k) & D_3(\mathsf{Q}^k) \end{bmatrix} C,$$

$$C(\mathsf{W}^k) = \begin{bmatrix} D_1(\mathsf{W}^k) & D_2(\mathsf{W}^k) & D_3(\mathsf{W}^k) \end{bmatrix} C.$$

After solving for F and G, we compute T^k via (47) or (48). This yields the finite element function $\mathbf{t}_h^k$ in Step (a) of Section 3.2.3.

4.6. Experimental order of convergence

We test the accuracy of our method against an exact solution found in [32, Sec. 6.4] that represents a plane defect (see Fig. 3). The computational domain is a cube $\Omega = [0, 1]^3$ and we set $\kappa = 0.2$. The double well potential is removed, so the energy is $E[s, \mathbf{n}] \equiv E_1[s, \mathbf{n}]$.

The following Dirichlet boundary conditions on $\overline{\partial \Omega} \cap (\{z = 0\} \cup \{z = 1\})$ are imposed for $(s, \mathbf{n})$:

$$\begin{aligned} z = 0: \quad s = s^*, \qquad \mathbf{n} = (1, 0, 0), \\ z = 1: \quad s = s^*, \qquad \mathbf{n} = (0, 1, 0), \end{aligned} \tag{54}$$

and Neumann conditions are imposed on the remaining part of $\partial \Omega$, i.e. $\boldsymbol{\nu} \cdot \nabla s = 0$ and $\boldsymbol{\nu} \cdot \nabla \mathbf{n} = 0$. The exact solution $(s, \mathbf{n})$ (at equilibrium) only depends on z and is given by

$$\begin{aligned} \mathbf{n}(z) = (1, 0, 0), \text{ for } z < 0.5, \quad \mathbf{n}(z) = (0, 1, 0), \text{ for } z > 0.5, \\ s(z) = 0, \text{ at } z = 0.5, \text{ and } s(z) \text{ is linear for } z \in (0, 0.5) \cup (0.5, 1.0). \end{aligned} \tag{55}$$

Fig. 3 gives an illustration of $\mathbf{n}$, and Fig. 4 shows a one-dimensional slice of s.

Numerical errors are given in Table 1. The meshes were created by partitioning Ω into $(2^\ell)^3$ uniform cubes, where ℓ is the mesh level, and sub-dividing each cube into six non-obtuse tetrahedra. The estimated order of convergence is given in the last row of the table. The L^2-accuracy appears to be first order for both $(s, \mathbf{u})$, the smoother variables, and half order for $\mathbf{n}$. Since $\mathbf{n}$ is discontinuous across the plane $\{x_3 = 0\}$ (plane defect), we cannot expect better accuracy in L^2 with continuous elements; moreover, s does not have better regularity than H^1. Furthermore, our discrete energy E_1^h uses a first order approximation (16) of $\int_\Omega s^2 |\nabla \mathbf{n}|^2$, which is accounted for by the consistency errors (21). These two facts are most likely responsible for the reduced linear order for $(s, \mathbf{u})$.
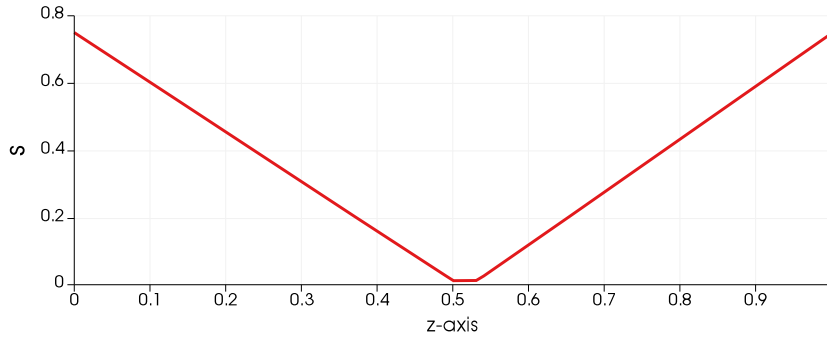
Fig. 4. Simulation results for Section 4.6. The scalar field s is shown evaluated along a line parallel to the z-axis and passing through $x = 0.5$, $y = 0.5$. It is close to the exact piecewise linear solution in (55). The numerical solution was computed at mesh level $\ell = 5$.

Table 1
Numerical error vs. mesh refinement for plane defect in three dimensions. The estimated order of convergence (EOC) is given in the last row.

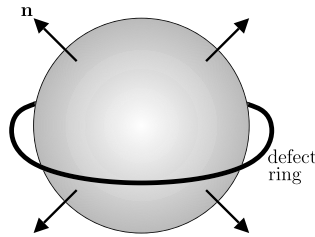| Level ℓ	$\|s - s_h\|_{L^2(\Omega)}$	$\|s - s_h\|_{H^1(\Omega)}$	$\|\mathbf{n} - \mathbf{n}_h\|_{L^2(\Omega)}$	$\|\mathbf{u} - \mathbf{u}_h\|_{L^2(\Omega)}$	$\|\mathbf{u} - \mathbf{u}_h\|_{H^1(\Omega)}$
3	5.5087E−02	5.5090E−01	2.6693E−01	5.7355E−02	4.6602E−01
4	2.9158E−02	3.9858E−01	2.0545E−01	2.9840E−02	3.2646E−01
5	1.4981E−02	2.7986E−01	1.4642E−01	1.5207E−02	2.2661E−01
6	7.5964E−03	1.9726E−01	1.0398E−01	7.6800E−03	1.5878E−01
EOC	0.9797	0.5046	0.4938	0.9855	0.5132

Fig. 5. Illustration of the Saturn ring defect. A spherical colloidal particle is shown with normal anchoring conditions on its boundary (i.e. the director field **n** is parallel to the normal vector ν of the sphere). The region where $s = 0$ (i.e. the singular set $\mathbb{S}$) is marked by the thick curve and occurs depending on the outer boundary conditions (away from the sphere) imposed on **n**.

5. Colloidal effects

Colloidal particles immersed in a liquid crystal can induce interesting equilibrium states with non-trivial defect configurations. One example is the famous Saturn ring defect [68,84], which is a circular ring of defect surrounding a spherical hole inside the liquid crystal domain (see Fig. 5), i.e. Ω is the region outside the sphere.

In this section, we demonstrate that the Ericksen model and our numerical method are able to capture interesting defect structures in the presence of colloids. The colloid particle is modeled as a spherical inclusion inside the liquid crystal domain. Section 5.1 shows a direct simulation (with a conforming mesh) which gives rise to a Saturn ring-like defect structure (depending on outer boundary conditions). In Section 5.2, we combine our method for the Ericksen model with an immersed boundary approach and compare with our conforming mesh approach. For both subsections, we use the following notation. The liquid crystal domain is denoted by Ω, with boundary $\partial\Omega$ that decomposes into a disjoint union $\partial\Omega = \Gamma_i \cup \Gamma_o$, where Γ_i is the boundary of the interior "hole" and Γ_o is the outer boundary of the cylindrical domain that contains the hole (see Figs. 8 and 11).

5.1. Conforming non-obtuse mesh

5.1.1. Meshing the domain

It is quite difficult to generate a conforming, **non-obtuse**, tetrahedral mesh of a general domain; in fact, it is still an open question whether it is always possible to generate a non-obtuse tetrahedral mesh of a general three dimensional domain. For our purposes, we managed to create a non-obtuse mesh of a cylindrical domain with a hole cut out, but the procedure is not general. However, the resulting mesh is valid for testing our method.

We start by describing the domain Ω, which is essentially a cylinder with square cross-section with a spherical hole removed from the interior. First, we create a tetrahedral mesh of a rectangular solid with the following dimensions:
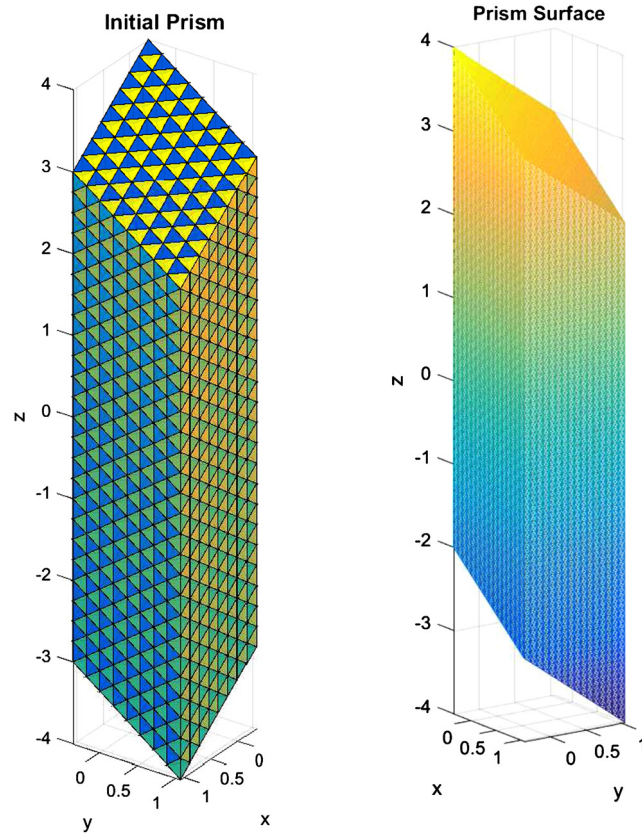
Fig. 6. Non-obtuse mesh of cylindrical domain with interior spherical hole. Left figure depicts the initial mesh obtained by first partitioning a right prism into $8 \times 8 \times 24$ cubes and dividing them into six tetrahedra, and next mapping them via (56). Right picture (rotated 90 degrees) displays the final mesh, with 1,764,864 tetrahedra, after applying a 1-to-8 refinement and a 1-to-24 "yellow" refinement to the previous mesh. (For interpretation of the references to color in this figure legend, the reader is referred to the web version of this article.)

$[-0.5, 1.5] \times [-0.5, 1.5] \times [-2.5, 3.5]$. We partition the solid into $8 \times 8 \times 24$ uniformly sized cubes, of side length $h = 0.25$, and further partition each cube into six tetrahedra.

Next, we shear the mesh by mapping the vertices with the following linear map:

$$\mathbf{x} = \begin{bmatrix} x \\ y \\ z \end{bmatrix} = \begin{bmatrix} 1/\sqrt{2} & 0 & 0 \\ 0 & 1/\sqrt{2} & 0 \\ -1/2 & -1/2 & 1 \end{bmatrix} \hat{\mathbf{x}}, \tag{56}$$

where $\hat{\mathbf{x}}$ are coordinates in the initial rectangular solid. This results in a mesh of so-called *ideal* tetrahedra, whose circumcenters coincide with their barycenters [85,86] (so-called "well-centered" tetrahedra). The resulting "prism" is a cylinder with square cross-section given by $[-0.25\sqrt{2}, 0.75\sqrt{2}]^2$ and is centered about the $z = 0$ plane (see Fig. 6).

We then remove all tetrahedra (from the prism mesh) whose circumcenters are inside a sphere of radius $R = 0.283/\sqrt{2}$ centered at $(0.5/\sqrt{2}, 0.5/\sqrt{2}, 0)^T$. The internal cavity represents our spherical colloid. We make a small adjustment of the vertex positions on the boundary of the cavity so that they lie exactly on the given sphere boundary. Thus, the tetrahedra are slightly off from being exactly well-centered.

In order to have a more accurate simulation, we apply two well chosen refinements in the following way. We use a standard 1-to-8 uniform refinement of the mesh [87], while choosing the best diagonal to maintain the well-centered property. The (new) vertices on the boundary of the internal cavity are *adjusted* so that the mesh conforms to the sphere. The resulting mesh is not as well-centered, but all tetrahedra still strictly contain their circumcenters. Therefore, we use the "yellow" refinement described in [88, pg. 1108–1109], which partitions each tetrahedron into 24 tetrahedra where each new tetrahedron has the circumcenter as a vertex. This final refinement is guaranteed to yield a non-obtuse mesh; see Fig. 6 for a view of the surface mesh of the prism.

Note that we do not adjust the new vertices (generated by the second refinement) to lie on the spherical hole's boundary. Any adjustment seems to yield an obtuse mesh, because the domain with hole is not convex. Thus, the surface mesh of the internal spherical hole boundary is slightly faceted (see Fig. 7). This is allowable because the defect structures of interest are not very sensitive to the fine details of the geometry of the hole.
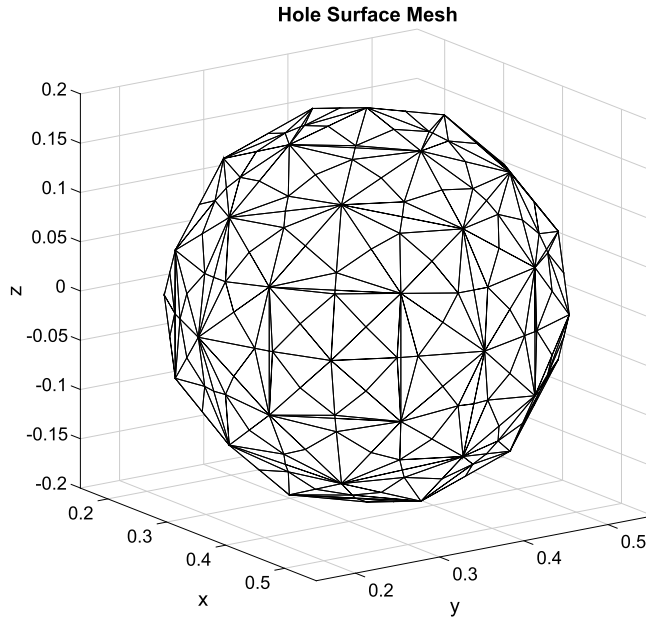
Hole Surface Mesh

Fig. 7. Surface mesh of the interior hole. Not all vertices lie on the spherical cavity, so as to ensure that all tetrahedra are non-obtuse, thereby giving a slightly faceted surface mesh. This is compatible with the Saturn ring defect not being very sensitive to fine details of the hole geometry.
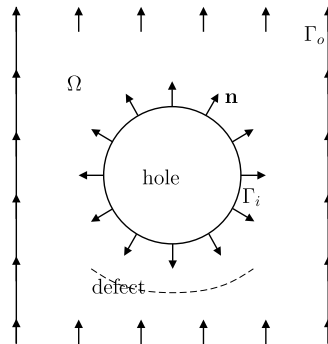

Fig. 8. Boundary conditions for a disperse/point defect (Section 5.1.2). One can see why a defect arises because of the incompatibility of the director fields on the bottom of the sphere and the bottom of the prism.

The final mesh has 1,764,864 tetrahedra and 329,698 vertices. The dihedral angles are between $4.156°$ and $90°$ (non-obtuse); the surface mesh angles are between $2.726°$ and $90°$. The minimum angles are not great, but acceptable for numerical simulation.

5.1.2. Simulating a disperse/point defect

Consider the boundary conditions shown in Fig. 8, which is the director field version of the Landau–deGennes model considered in [84]. The precise strong anchoring condition is given by

$$\mathbf{n} = \mathbf{\nu}, \text{ on } \Gamma_i, \quad \mathbf{n} = (0, 0, 1)^T, \text{ on } \Gamma_o, \quad s = s^*, \text{ on } \partial\Omega, \tag{57}$$

where $\mathbf{\nu}$ is the outer normal vector of the spherical inclusion, and s^* is the global minimum of the double well potential ψ. Moreover, the double well potential has the convex splitting $\psi(s) = (0.3)^{-2} (\psi_c(s) - \psi_e(s))$ for $-\frac{1}{2} < s < 1$, where

$$\psi_c(s) := 63.0s^2 \qquad \psi_e(s) := -16.0s^4 + 21.33333333333s^3 + 57.0s^2, \tag{58}$$

with a local minimum at $s = 0$ and global minimum at $s = s^* := 0.750025$. The initial conditions in Ω for the gradient flow are: $s = s^*$ and $\mathbf{n} = (0, 0, 1)^T$.

The equilibrium solution, for $\kappa = 0.1$, is shown in Fig. 9. The low value of κ leads to a large disperse defect region, which is induced by the "frustrated" boundary conditions between the bottom of the sphere and the bottom of the cylinder (see Fig. 8).
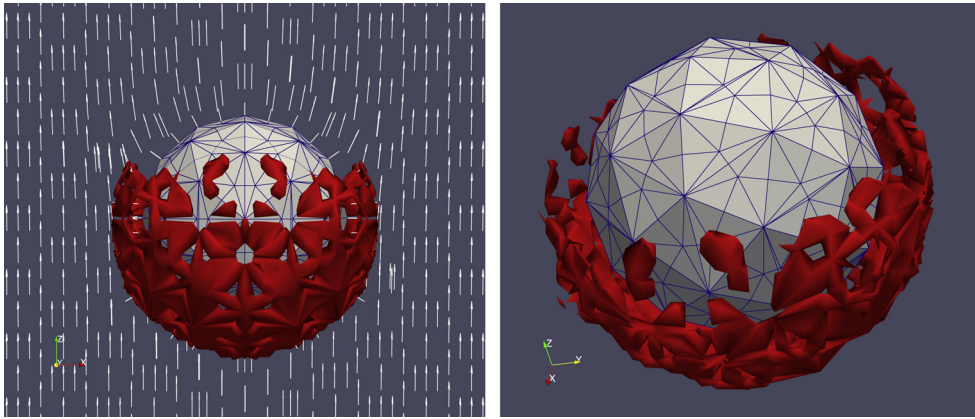
Fig. 9. Simulation results for Fig. 8 ($\kappa = 0.1$). The surface mesh of the internal hole is shown and the $s = 0.04$ iso-surface is plotted in red which indicates the defect region; the director field is depicted with white arrows. The disperse defect region has a bowl-like shape underneath the internal hole. (For interpretation of the references to color in this figure legend, the reader is referred to the web version of this article.)
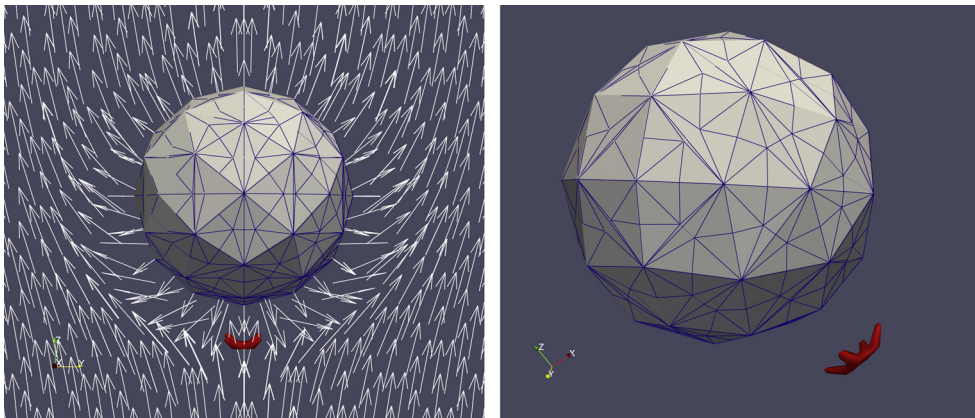

Fig. 10. Simulation results for Fig. 8 ($\kappa = 1.0$). The surface mesh of the internal hole is shown and the $s = 0.1$ iso-surface is plotted in red which indicates the defect region; the director field is depicted with white arrows. The defect region is more localized to a "point" below the internal hole (cf. Fig. 9). (For interpretation of the references to color in this figure legend, the reader is referred to the web version of this article.)

A different equilibrium solution is obtained with $\kappa = 1.0$, which is shown in Fig. 10. The larger value of κ leads to a smaller defect region compared to Fig. 9. The center of the hole is $\approx (0.354, 0.354, 0)^T$ and the location of the defect region is $\approx (0.354, 0.354, -0.275)^T$.

5.1.3. Simulating a Saturn ring-like defect

Consider the boundary conditions shown in Fig. 11, which is another director field version of the Landau–deGennes model considered in [84]. The strong anchoring condition is given by

$$\mathbf{n} = \boldsymbol{\nu}, \text{ on } \Gamma_i, \quad s = s^*, \text{ on } \partial\Omega, \tag{59}$$

where $\mathbf{n}$ smoothly interpolates between $(0, 0, -1)^T$ and $(0, 0, 1)^T$ on Γ_o. The same double well potential is used as in (58). The initial conditions in Ω for the gradient flow are: $s = s^*$ and

$$\mathbf{n}(x, y, z) = (0, 0, -1)^T, \text{ if } z < 0,$$
$$\mathbf{n}(x, y, z) = (0, 0, +1)^T, \text{ if } z \geq 0.$$

The equilibrium solution, for $\kappa = 1.0$, is shown in Fig. 12. The choice of boundary conditions in Fig. 11 essentially induces the Saturn ring defect. The hole's radius is ≈ 0.200111 and the radius of the Saturn ring is ≈ 0.314. Note that the structure of the director field is not the same as would be obtained with the Landau–deGennes model [84]. For instance, the line field in the Saturn ring defect structure of [84] displays a 1/2 degree point defect, whereas in our model the point defect of the director field is of degree 1 (see Fig. 11). This is a limitation of the Ericksen's model, which is sensitive to the orientation of the director field $\mathbf{n}$.
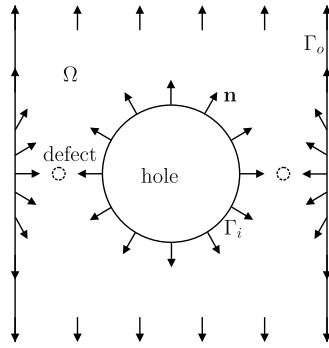
Fig. 11. Boundary conditions for Section 5.1.3. A ring-like defect arises in this case because the director field on the sides of the cylinder are incompatible with the director field on the sphere.
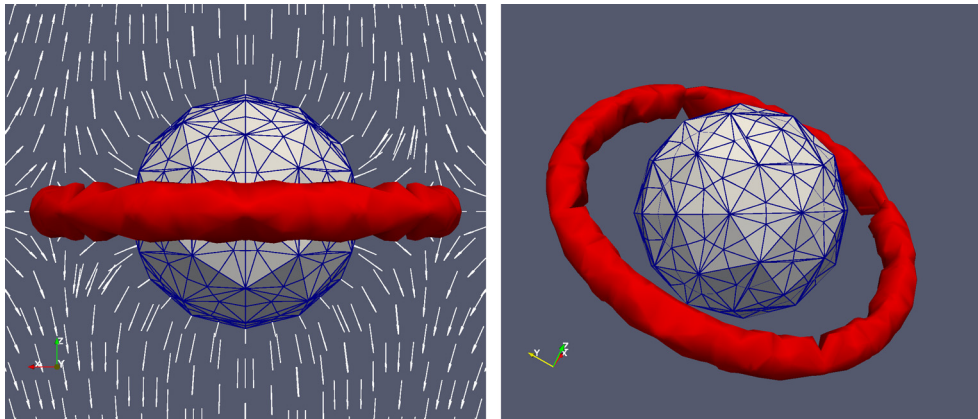

Fig. 12. Simulation results for Fig. 11 ($\kappa = 1.0$). The surface mesh of the internal hole is shown and the $s = 0.12$ iso-surface is plotted in red which indicates the defect region; the director field is depicted with white arrows. The defect region mimics the classic Saturn ring defect. (For interpretation of the references to color in this figure legend, the reader is referred to the web version of this article.)

5.2. Immersed boundary method

The weakly acute (or non-obtuse) condition on the mesh is extremely difficult to satisfy in practice in three dimensions. Therefore, we propose an immersed boundary approach to deal with general colloid shapes. We define a fixed "phase-field" function to represent the colloidal region inside the liquid crystal domain, and add a special "boundary" energy term E_a to enforce boundary conditions on the colloid's boundary. Specifically, we generalize the continuous (1) and discrete (16) total energies to

$$E[s, \mathbf{n}] := E_1[s, \mathbf{n}] + E_2[s] + E_a[s, \mathbf{n}], \tag{60}$$

$$E^h[s_h, \mathbf{n}_h] := E_1^h[s_h, \mathbf{n}_h] + E_2^h[s_h] + E_a^h[s_h, \mathbf{n}_h], \tag{61}$$

where E_a, E_a^h can take two different forms described in Sections 5.2.3 and 5.2.4.

5.2.1. Representing a colloid

Let $\Omega \subset \mathbb{R}^3$ be the "hold-all" domain that contains the liquid crystal material *and* colloids. Moreover, let $\hat{\Omega}_c \subset \mathbb{R}^3$ be the reference domain for a rigid solid (i.e. colloid), and let Ω_c be obtained from $\hat{\Omega}_c$ by a rigid motion. We use Ω_c to represent the true colloid domain, with $\hat{\Omega}_c$ as a reference shape. We assume throughout that $\Omega_c \subset\subset \Omega$. Thus, the region of interest for the liquid crystals is given by $\Omega \setminus \overline{\Omega_c}$.

Let $\hat{d} : \mathbb{R}^3 \to \mathbb{R}$ be the signed distance function to $\partial\hat{\Omega}_c$, i.e.

$$\hat{d}(\hat{\mathbf{x}}) = \text{dist}(\partial\hat{\Omega}_c, \hat{\mathbf{x}}), \quad \forall \hat{\mathbf{x}} \in \mathbb{R}^3, \tag{62}$$

which is positive inside of $\hat{\Omega}_c$; thus $\partial\hat{\Omega}_c$ is the zero level set of $\hat{d}$. Next, define an affine map $\mathbf{F} : \mathbb{R}^3 \to \mathbb{R}^3$ such that $\hat{\Omega}_c = \mathbf{F}(\Omega_c)$ by

$$\hat{\mathbf{x}} = \mathbf{F}(\mathbf{x}) = \mathbf{R}\mathbf{x} + \mathbf{b}, \tag{63}$$

where $\mathbf{R}$ is a constant rotation matrix, and $\mathbf{b}$ is a translation vector. Thus, the distance function for Ω_c is given by:

$$d(\mathbf{x}) = \hat{d}(\mathbf{F}(\mathbf{x})) = \hat{d}(\hat{\mathbf{x}}),$$
(64)

with derivative formula:

$$\nabla d(\mathbf{x}) = \hat{\nabla}\hat{d}(\mathbf{F}(\mathbf{x}))\nabla\mathbf{F}(\mathbf{x}) = \hat{\nabla}\hat{d}(\mathbf{F}(\mathbf{x}))\mathbf{R}.$$
(65)

5.2.2. Phase-field

Define a one dimensional phase-field function:

$$\phi_{\text{ref}}(t) = \frac{1}{2}\left[\frac{2}{\pi}\arctan\left(-\frac{t}{\epsilon}\right) + 1\right],$$
(66)

where $\phi_{\text{ref}} : (-\infty, \infty) \to (0, 1)$. The parameter $\epsilon > 0$ is the thickness of the transition. The derivative is given by:

$$\phi'_{\text{ref}}(t) = -\frac{1}{\pi\epsilon}\frac{1}{1 + \left(\frac{t}{\epsilon}\right)^2}.$$
(67)

The phase-field function associated with the colloidal sub-domain Ω_c is

$$\phi(\mathbf{x}) = \phi_{\text{ref}}(d(\mathbf{x})) = \phi_{\text{ref}}(\hat{d}(\mathbf{F}(\mathbf{x}))).$$
(68)

Thus, ϕ is essentially 0 inside the colloidal inclusion and 1 outside; so $\phi \approx 1$ "marks" where the liquid crystal domain is. The gradient is given by

$$\nabla\phi(\mathbf{x}) = \phi'_{\text{ref}}(d(\mathbf{x}))\nabla d(\mathbf{x}) = \phi'_{\text{ref}}(\hat{d}(\mathbf{F}(\mathbf{x})))\hat{\nabla}\hat{d}(\mathbf{F}(\mathbf{x}))\nabla\mathbf{F}(\mathbf{x})$$
$$= \phi'_{\text{ref}}(\hat{d}(\mathbf{F}(\mathbf{x})))\hat{\nabla}\hat{d}(\mathbf{F}(\mathbf{x}))\mathbf{R} = -\frac{1}{\pi\epsilon}\frac{1}{1 + \left(\frac{\hat{d}(\mathbf{F}(\mathbf{x}))}{\epsilon}\right)^2}\hat{\nabla}\hat{d}(\mathbf{F}(\mathbf{x}))\mathbf{R},$$
(69)

and so we have

$$|\nabla\phi(\mathbf{x})|^2 = \left(\frac{1}{\pi\epsilon}\right)^2\frac{1}{\left(1 + \left(\frac{\hat{d}(\mathbf{F}(\mathbf{x}))}{\epsilon}\right)^2\right)^2}|\hat{\nabla}\hat{d}(\mathbf{F}(\mathbf{x}))|^2.$$
(70)

We note the following relation between bulk and surface integrals. Given $f \in C(\overline{\Omega})$, define

$$J_\epsilon(f) = C_0\frac{\epsilon}{2}\int_\Omega f(\mathbf{x})|\nabla\phi(\mathbf{x})|^2 d\mathbf{x}, \quad \text{where } C_0 := 4\pi.$$
(71)

Then one can show that (since $|\hat{\nabla}\hat{d}(\cdot)| = 1$ near the zero level set of $\hat{d}(\cdot)$)

$$\lim_{\epsilon\to 0} J_\epsilon(f) = \int_{\partial\Omega_c} f(\mathbf{x})ds(\mathbf{x}).$$

In particular, $\lim_{\epsilon\to 0} J_\epsilon(1) = |\partial\Omega_c|$ is the surface area of the boundary of the colloid Ω_c.

5.2.3. Weak anchoring

We model boundary conditions on the colloid's surface by imposing *weak anchoring* [32,2] with E_a, E_a^h. A standard, but somewhat ad-hoc, form for the energy in the $\mathbf{Q}$-tensor model [89, eqn. (66)] is

$$J(\mathbf{Q}) = \frac{K_a}{2}\int_{\partial\Omega_c}|\mathbf{Q} - \mathbf{Q}_0|^2,$$
(72)

where $\mathbf{Q}_0$ is the desired value of $\mathbf{Q}$ on the boundary $\partial\Omega_c$ and K_a is a large weighting parameter (penalty approach). For our purposes, we will focus on imposing homeotropic anchoring, i.e. we take $\mathbf{Q}_0$ to have the form of a uniaxial nematic:

$$\mathbf{Q}_0 = s^*\left(\boldsymbol{\nu}\otimes\boldsymbol{\nu} - \frac{1}{3}\mathbf{I}\right),$$

where $\boldsymbol{\nu}$ is the normal of $\partial \Omega_c$ and s^* is the global minimum of the double well potential. Using the expression $\mathbf{Q} = s(\mathbf{n} \otimes \mathbf{n} - \frac{1}{3}\mathbf{I})$ for uniaxial nematics, along with the facts that $\mathbf{Q}, \mathbf{Q}_0$ are symmetric, $|\mathbf{Q} - \mathbf{Q}_0|^2 = \mathrm{tr}\left[(\mathbf{Q} - \mathbf{Q}_0)^2\right]$, and $|\mathbf{n}| = |\boldsymbol{\nu}| = 1$, a straightforward calculation gives

$$|\mathbf{Q} - \mathbf{Q}_0|^2 = 2ss^* \left[|\mathbf{n}|^2|\boldsymbol{\nu}|^2 - (\mathbf{n} \cdot \boldsymbol{\nu})^2\right] + \frac{2}{3}(s - s^*)^2|\boldsymbol{\nu}|^2. \tag{73}$$

We use (73) as motivation for our weak anchoring energy in the context of the Ericksen model combined with the immersed boundary method. In fact, noting that $\boldsymbol{\nu} = \nabla\phi/|\nabla\phi|$, simplifying ss^* in (73) with s^2, and normalizing the constants, we resort to (71) to define the continuous weak anchoring energy as

$$E_a[s, \mathbf{n}] := \frac{K_a}{2}C_0\epsilon \int_\Omega s^2 \left[|\mathbf{n}|^2|\nabla\phi|^2 - (\nabla\phi \cdot \mathbf{n})^2\right] + \frac{K_a}{2}C_0\epsilon \int_\Omega |\nabla\phi|^2(s - s^*)^2. \tag{74}$$

Note that (74) imposes normal anchoring of the director field when minimized. However, since (74) is invariant with respect to arbitrary changes in the sign of $\mathbf{n}$, we expect a different behavior of the director field $\mathbf{n}$ close to the colloid boundary $\partial \Omega_c$ from that in Section 5.1. This is confirmed by the numerical experiments of Subsection 5.2.6.

The next task is to modify the energies $E_1[s, \mathbf{n}]$ and $E_2[s]$ to account for the colloid, or equivalently for the phase variable ϕ. One possible choice is

$$E_1[s, \mathbf{n}] := \int_\Omega \phi \left(\kappa|\nabla s|^2 + s^2|\nabla\mathbf{n}|^2\right)dx, \qquad E_2[s] := \int_\Omega \phi\,\psi(s)dx, \tag{75}$$

which has the disadvantage that the system is near singular in Ω_c where $\phi \approx 0$ and still requires values for $\mathbf{n}$ and s inside Ω_c. We thus prefer to take a extreme approach and think of the colloid Ω_c as a rigid membrane filled with liquid crystal material and subjected to the same weak anchoring condition as the exterior. In the limit $\epsilon \to 0$, the two systems inside and outside of Ω_c decouple and we may simply consider the latter. This suggests keeping the original forms for E_1 and E_2 in (2). Therefore, we use the continuous total energy in (60).

We now discuss the discrete counterpart of (60), starting with $E_a[s, \mathbf{n}]$. We first introduce the following discrete inner products:

$$a_h^{\mathbf{n}}(\mathbf{n}_h, \mathbf{v}_h; s_h, \nabla\phi) := \int_\Omega I_h\left\{s_h^2\left[(\mathbf{n}_h \cdot \mathbf{v}_h)|\nabla\phi|^2 - (\nabla\phi \cdot \mathbf{n}_h)(\nabla\phi \cdot \mathbf{v}_h)\right]\right\},$$

$$a_h^S(s_h, z_h; \mathbf{n}_h, \nabla\phi) := \int_\Omega I_h\left\{s_h z_h\left[|\mathbf{n}_h|^2|\nabla\phi|^2 - (\nabla\phi \cdot \mathbf{n}_h)^2\right]\right\}, \tag{76}$$

where I_h is the Lagrange interpolant. These expressions correspond to using so-called mass lumping quadrature which, for all $f \in C^0(\overline{\Omega})$, reads

$$\int_\Omega I_h f = \sum_{T \in \mathcal{T}_h} \int_T I_h f = \sum_{T \in \mathcal{T}_h} \frac{|T|}{d + 1} \sum_{i=1}^{d+1} f(x_T^i), \tag{77}$$

where $\{x_T^i\}_{i=1}^{d+1}$ are the vertices of T. This quadrature rule is exact for piecewise linear polynomials and has the advantage that the finite element realization of (76) is a *diagonal* matrix. The following result elaborates on this.

Lemma 6 (*Monotone property for lumped mass matrix*). *Let $m_h : \mathbb{U}_h \times \mathbb{U}_h \to \mathbb{R}$ be a bilinear form defined by*

$$m_h(\mathbf{n}_h, \mathbf{v}_h) := \int_\Omega I_h\left[\mathbf{n}_h \cdot H(x)\mathbf{v}_h\right]dx,$$

where H is a continuous $d \times d$ symmetric positive semi-definite matrix. If $|\mathbf{n}_h(x_i)| \geq 1$ at all nodes x_i in $\mathcal{N}_h$, then

$$m_h(\mathbf{n}_h, \mathbf{n}_h) \geq m_h\left(\frac{\mathbf{n}_h}{|\mathbf{n}_h|}, \frac{\mathbf{n}_h}{|\mathbf{n}_h|}\right).$$

Proof. In view of (77), we rewrite $m_h(\mathbf{n}_h, \mathbf{v}_h)$ as

$$m_h(\mathbf{n}_h, \mathbf{v}_h) = \sum_{T \in \mathcal{T}_h} \frac{|T|}{d + 1} \sum_{i=1}^{d+1} \left[\mathbf{n}_h(x_T^i) \cdot H(x_T^i)\mathbf{v}_h(x_T^i)\right].$$

Then, clearly

$$
\begin{aligned}
m_h(\mathbf{n}_h, \mathbf{n}_h) &= \sum_{T \in \mathcal{T}_h} \frac{|T|}{d+1} \sum_{i=1}^{d+1} |\mathbf{n}_h(x_T^i)|^2 \left[\frac{\mathbf{n}(x_T^i)}{|\mathbf{n}_h(x_T^i)|} \cdot H(x_T^i) \frac{\mathbf{n}_h(x_T^i)}{|\mathbf{n}_h(x_T^i)|} \right] \\
&\geq \sum_{T \in \mathcal{T}_h} \frac{|T|}{d+1} \sum_{i=1}^{d+1} \left[\frac{\mathbf{n}_h(x_T^i)}{|\mathbf{n}_h(x_T^i)|} \cdot H(x_T^i) \frac{\mathbf{n}_h(x_T^i)}{|\mathbf{n}_h(x_T^i)|} \right] = m_h \left(\frac{\mathbf{n}_h}{|\mathbf{n}_h|}, \frac{\mathbf{n}_h}{|\mathbf{n}_h|} \right),
\end{aligned}
$$

which concludes the proof. □

To apply Lemma 6 to the first bilinear form in (76) we observe that H reads

$$
H = s_h^2 \Big(|\nabla \phi|^2 \mathbf{I} - \nabla \phi \otimes \nabla \phi \Big),
$$

and is symmetric positive semi-definite, whence

$$
a_h^{\mathbf{n}}(\mathbf{n}_h, \mathbf{n}_h; s_h, \nabla \phi) \geq a_h^{\mathbf{n}} \left(\frac{\mathbf{n}_h}{|\mathbf{n}_h|}, \frac{\mathbf{n}_h}{|\mathbf{n}_h|}; s_h, \nabla \phi \right). \tag{78}
$$

Thus, we take the discrete weak anchoring energy to be

$$
E_a^h[s_h, \mathbf{n}_h] := \frac{K_a}{2} C_0 \epsilon \left(a_h^{\mathbf{n}}(\mathbf{n}_h, \mathbf{n}_h; s_h, \nabla \phi) + \int_\Omega |I_h \nabla \phi|^2 (s_h - s^*)^2 \right); \tag{79}
$$

note that $a_h^{\mathbf{n}}(\mathbf{n}_h, \mathbf{n}_h; s_h, \nabla \phi) = a_h^s(s_h, s_h; \mathbf{n}_h, \nabla \phi)$. The discrete total energy is then given by (61).

5.2.4. Penalizing Dirichlet conditions

The weak anchoring energy (74) is insensitive to the orientation of the director field $\mathbf{n}$, a drawback of this approach for the Ericksen model. To impose a general Dirichlet boundary condition $(g, \mathbf{r})$ on the colloid's surface, in a more consistent manner, we consider a different penalization.

Consider the following penalization energy:

$$
J[s, \mathbf{u}] = \frac{K_a}{2} \int_{\partial \Omega_c} |\mathbf{u} - \mathbf{r}|^2 + |s - g|^2,
$$

where K_a is a large penalty parameter. We proceed as in Section 5.2.3, that is we first manipulate this formula to get one with suitable monotonicity properties. Write $\mathbf{u} = s\mathbf{n}$ and $\mathbf{r} = g\boldsymbol{\nu}$, replace g by s because $s \approx g$, and expand the first square using that $|\mathbf{n}| = |\boldsymbol{\nu}| = 1$ to get $|\mathbf{u} - \mathbf{r}|^2 = s^2 |\mathbf{n} - \boldsymbol{\nu}|^2$. We next express the line energy $J[s, \mathbf{u}]$ as a bulk energy within the immerse boundary method. Recall that $\boldsymbol{\nu} = \nabla \phi / |\nabla \phi|$ and make use of (71) to define

$$
E_a[s, \mathbf{n}] := \frac{K_a}{2} C_0 \epsilon \int_\Omega |\nabla \phi|^2 \left\{ s^2 \left| \mathbf{n} - \frac{\nabla \phi}{|\nabla \phi|} \right|^2 + |s - g|^2 \right\}. \tag{80}
$$

The discrete form of this penalized Dirichlet energy is given by

$$
E_a^h[s_h, \mathbf{n}_h] := \frac{K_a}{2} C_0 \epsilon \left(\widetilde{a}_h^s(s_h, s_h; \mathbf{n}_h, \nabla \phi) + \int_\Omega |I_h \nabla \phi|^2 (s_h - g_h)^2 \right), \tag{81}
$$

where

$$
\begin{aligned}
\widetilde{a}_h^{\mathbf{n}}(\mathbf{n}_h, \mathbf{v}_h; s_h, \nabla \phi) &:= \int_\Omega I_h \left\{ s_h^2 |\nabla \phi|^2 \mathbf{n}_h \cdot \mathbf{v}_h \right\}, \\
\ell_h(\mathbf{v}_h; s_h, \nabla \phi) &:= \int_\Omega I_h \left\{ s_h^2 |\nabla \phi| \nabla \phi \cdot \mathbf{v}_h \right\}, \\
\widetilde{a}_h^s(s_h, z_h; \mathbf{n}_h, \nabla \phi) &:= \int_\Omega I_h \left\{ s_h z_h \big| |\nabla \phi| \mathbf{n}_h - \nabla \phi \big|^2 \right\}.
\end{aligned} \tag{82}
$$

Note that

$$\widetilde{a}_h{}^s(s_h, s_h; \mathbf{n}_h, \nabla\phi) = \widetilde{a}_h{}^{\mathbf{n}}(\mathbf{n}_h, \mathbf{n}_h; s_h, \nabla\phi) - 2\ell_h(\mathbf{n}_h; s_h, \nabla\phi) + \int_\Omega I_h\left\{s_h^2|\nabla\phi|^2\right\}, \tag{83}$$

and that $\widetilde{a}_h{}^{\mathbf{n}}$ and $\ell_h(\mathbf{v}_h; s_h, \nabla\phi)$ are also useful in computing variational derivatives of (81). Recall that the total discrete energy is given by (61). The presence of the Lagrange interpolation operator I_h in (81), (82) is needed to ensure that Step 2 (projection) of the Algorithm in Subsection 3.2.3 decreases the energy (see (84) below).

Lemma 7 (*Monotone property for penalized Dirichlet energy*). *Let $d \geq 2$ and let $\mathbf{n}, \mathbf{m}$ be arbitrary vectors in $\mathbb{S}^{d-1}$. If $\mathbf{t} \in \mathbb{R}^d$ such that $|\mathbf{n} + \mathbf{t}| \geq 1$, then*

$$|(\mathbf{n} + \mathbf{t}) - \mathbf{m}| \geq \left|\frac{\mathbf{n} + \mathbf{t}}{|\mathbf{n} + \mathbf{t}|} - \mathbf{m}\right|.$$

Proof. Let $\mathbf{n}_0 := \frac{\mathbf{n}+\mathbf{t}}{|\mathbf{n}+\mathbf{t}|}$ and note that

$$|(\mathbf{n} + \mathbf{t}) - \mathbf{m}|^2 = |\mathbf{n} + \mathbf{t}|^2 + 1 - 2\,\mathbf{n}_0 \cdot \mathbf{m}\,|\mathbf{n} + \mathbf{t}|, \qquad |\mathbf{n}_0 - \mathbf{m}|^2 = 2 - 2\,\mathbf{n}_0 \cdot \mathbf{m}.$$

This implies

$$|(\mathbf{n} + \mathbf{t}) - \mathbf{m}|^2 - |\mathbf{n}_0 - \mathbf{m}|^2 = |\mathbf{n} + \mathbf{t}|^2 - 1 - 2\,\mathbf{n}_0 \cdot \mathbf{m}\big(|\mathbf{n} + \mathbf{t}| - 1\big)$$
$$= \big(|\mathbf{n} + \mathbf{t}| - 1\big)\big(|\mathbf{n} + \mathbf{t}| + 1 - 2\mathbf{n}_0 \cdot \mathbf{m}\big) \geq 0,$$

because $|\mathbf{n} + \mathbf{t}| \geq 1$. This is the asserted estimate. $\quad\square$

We now apply Lemma 7 to $\widetilde{a}_h{}^s$ in (81), by setting $\mathbf{m} = \nabla\phi/|\nabla\phi|$, and obtain the monotonicity property

$$\widetilde{a}_h{}^s(s_h, s_h; \mathbf{n}_h + \mathbf{t}_h, \nabla\phi) = \int_\Omega I_h\left\{|\nabla\phi|^2 s_h^2\left|(\mathbf{n}_h + \mathbf{t}_h) - \frac{\nabla\phi}{|\nabla\phi|}\right|^2\right\}$$
$$\geq \widetilde{a}_h{}^s\left(s_h, s_h; \frac{\mathbf{n}_h + \mathbf{t}_h}{|\mathbf{n}_h + \mathbf{t}_h|}, \nabla\phi\right), \tag{84}$$

where it is assumed that $\mathbf{n}_h(x_i) \cdot \mathbf{t}_h(x_i) = 0$ at all nodes x_i.

5.2.5. Minimization scheme

We apply the Algorithm in Section 3.2.3 to the total energy (61) in the case of either weak anchoring energy (79) or penalized Dirichlet energy (81). To this end, we need the following additional variational derivatives of E_a^h. The first order variation of $E_a^h[s_h, \mathbf{n}_h]$ in the direction $\mathbf{v}_h \in \mathbb{U}_h^\perp(\mathbf{n}_h^k) \cap H_{\Gamma_{\mathbf{n}}}^1(\Omega)$ at the director variable $\mathbf{n}_h^k$ reads

$$\delta_{\mathbf{n}_h} E_a^h[s_h^k, \mathbf{n}_h^k; \mathbf{v}_h] = K_a C_0 \epsilon\, a_h^{\mathbf{n}}(\mathbf{n}_h^k, \mathbf{v}_h; s_h^k, \nabla\phi), \tag{85}$$

for the energy (79), whereas the expression reads

$$\delta_{\mathbf{n}_h} E_a^h[s_h^k, \mathbf{n}_h^k; \mathbf{v}_h] = K_a C_0 \epsilon\left\{\widetilde{a}_h{}^{\mathbf{n}}(\mathbf{n}_h^k, \mathbf{v}_h; s_h^k, \nabla\phi) - \ell_h(\mathbf{v}_h; s_h^k, \nabla\phi)\right\}, \tag{86}$$

for the energy (81).

The first order variation of $E_a^h[s_h, \mathbf{n}_h]$ in the direction $z_h \in \mathbb{S}_h \cap H_{\Gamma_s}^1(\Omega)$ at the degree of orientation variable s_h^k is

$$\delta_{s_h} E_a^h[s_h^k, \mathbf{n}_h^k; z_h] = K_a C_0 \epsilon\left\{a_h^s(s_h^k, z_h; \mathbf{n}_h^k, \nabla\phi) + \int_\Omega |I_h\nabla\phi|^2(s_h^k - s^*)z_h\right\} \tag{87}$$

for the energy (79), whereas the expression reads

$$\delta_{s_h} E_a^h[s_h^k, \mathbf{n}_h^k; z_h] = K_a C_0 \epsilon\left\{\widetilde{a}_h{}^s(s_h^k, z_h; \mathbf{n}_h^k, \nabla\phi) + \int_\Omega |I_h\nabla\phi|^2(s_h^k - g_h)z_h\right\} \tag{88}$$

for the energy (81). Note that (78) and (84) guarantee that the projection step in our algorithm reduces the energy $E_a^h[s_h, \mathbf{n}_h]$, whence Theorem 3 still holds in this context (see Theorem 8).
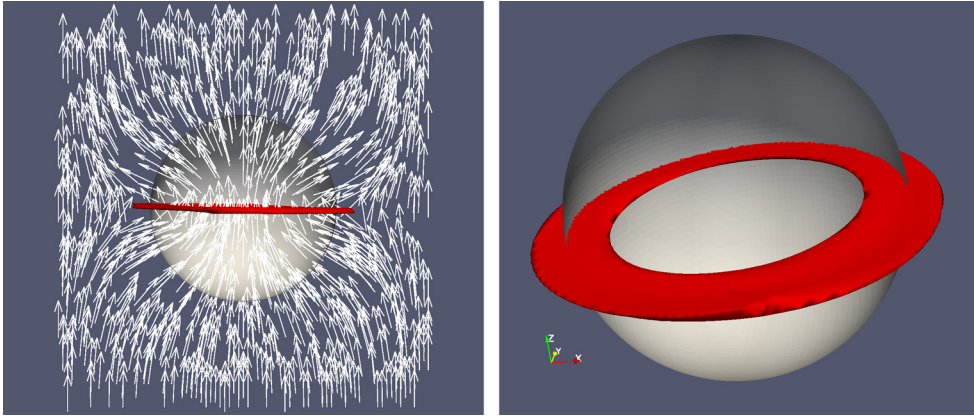
Fig. 13. Simulation results for boundary conditions in (89) ($\kappa = 1.0$) using the immersed boundary approach and anchoring energy (79). The surface mesh of the colloid boundary is shown and the $s = 0.14$ iso-surface is plotted in red which indicates the defect region. The director field is also shown (white arrows) on a plane parallel to the y–z plane and passing through $x = 0.5$. The defect region is spread out into a "washer" region (cf. Section 5.1.2). (For interpretation of the references to color in this figure legend, the reader is referred to the web version of this article.)

5.2.6. Simulating defects with weak anchoring

The computational domain is a unit cube $\Omega = [0, 1]^3$. The colloid is represented by a sphere of radius 0.25 centered at $(0.5, 0.5, 0.5)^T$. We consider the boundary conditions shown in Fig. 8. The strong anchoring condition on $\partial\Omega$ is given by

$$\mathbf{n} = (0, 0, 1)^T, \text{ on } \partial\Omega, \quad s = s^*, \text{ on } \partial\Omega, \tag{89}$$

whereas E_a given in (79) models weak anchoring on the colloid's surface with parameters

$$K_a = 300.0, \qquad \epsilon = 0.06.$$

We use the same double well potential as before. The initial conditions in Ω for the gradient flow are: $s = s^*$ and $\mathbf{n} = (0, 0, 1)^T$.

The equilibrium solution, with $\kappa = 1.0$, is shown in Fig. 13. The defect region is significantly different than that shown in Section 5.1.2. This is due to the fact that the weak anchoring energy (74) is invariant with respect to arbitrary changes in the sign of $\mathbf{n}$.

Next, we change the boundary conditions as we did in Section 5.1.3, i.e. the strong anchoring condition on $\partial\Omega$ is given by

$$\mathbf{n} \text{ smoothly interpolates between } (0, 0, -1)^T \text{ and } (0, 0, 1)^T, \text{ and } s = s^*, \text{ on } \partial\Omega, \tag{90}$$

whereas E_a models weak anchoring on the colloid's surface. The initial conditions in Ω for the gradient flow are: $s = s^*$ and

$$\mathbf{n}(x, y, z) = \begin{cases} (0, 0, -1)^T, & \text{if } z < 0, \\ (0, 0, +1)^T, & \text{if } z \geq 0. \end{cases}$$

The equilibrium solution, with $\kappa = 1.0$, is shown in Fig. 14. Again, the choice of boundary conditions essentially induces the Saturn ring defect. The radius of the Saturn ring is ≈ 0.38. Also, note that the structure of the director field is not the same as would be obtained with the Landau–deGennes model [84].

5.2.7. Simulating defects with penalized Dirichlet conditions

We adopt the same computational conditions here, except that E_a is given by (81) which models a Dirichlet condition (penalized) on the colloid's surface. Everything else is the same as before, including parameter values.

Using the first set of boundary conditions (89), the equilibrium solution ($\kappa = 1.0$) is shown in Fig. 15. The defect region is essentially the same as in Section 5.1.2 (see Fig. 10). In other words, the penalized Dirichlet condition is *not* invariant with respect to arbitrary changes in the sign of $\mathbf{n}$.

Next, we change the outer boundary conditions as we did in Section 5.1.3. Using the second set of boundary conditions (90), the equilibrium solution ($\kappa = 1.0$) is shown in Fig. 16.

The choice of boundary conditions induces the Saturn ring defect (similar to Fig. 12). The radius of the Saturn ring is ≈ 0.405. Also, note that the structure of the director field is not the same as would be obtained with the Landau–deGennes model [84].
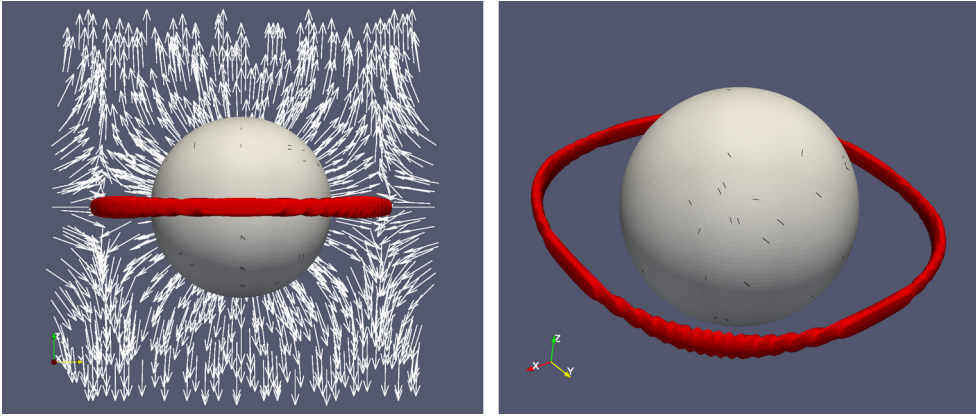
Fig. 14. Simulation results for boundary conditions in (90) ($\kappa = 1.0$) using the immersed boundary approach and anchoring energy (79). The surface mesh of the colloid boundary is shown and the $s = 0.06$ iso-surface is plotted in red which indicates the defect region. The director field is also shown (white arrows) on a plane parallel to the y–z plane and passing through $x = 0.5$. The defect region mimics the classic Saturn ring defect (cf. Section 5.1.3). (For interpretation of the references to color in this figure legend, the reader is referred to the web version of this article.)
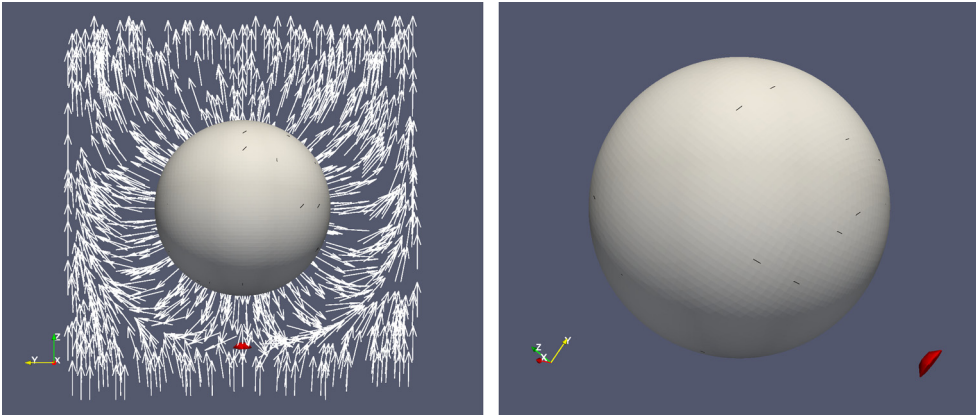

Fig. 15. Simulation results for boundary conditions in (89) ($\kappa = 1.0$) using the immersed boundary approach and anchoring energy (81). The surface mesh of the colloid boundary is shown and the $s = 0.06$ iso-surface is plotted in red which indicates the defect region. The director field is also shown (white arrows) on a plane parallel to the y–z plane and passing through $x = 0.5$. The defect region is "point-like" at height $z = 0.11$ (cf. Section 5.1.2). (For interpretation of the references to color in this figure legend, the reader is referred to the web version of this article.)
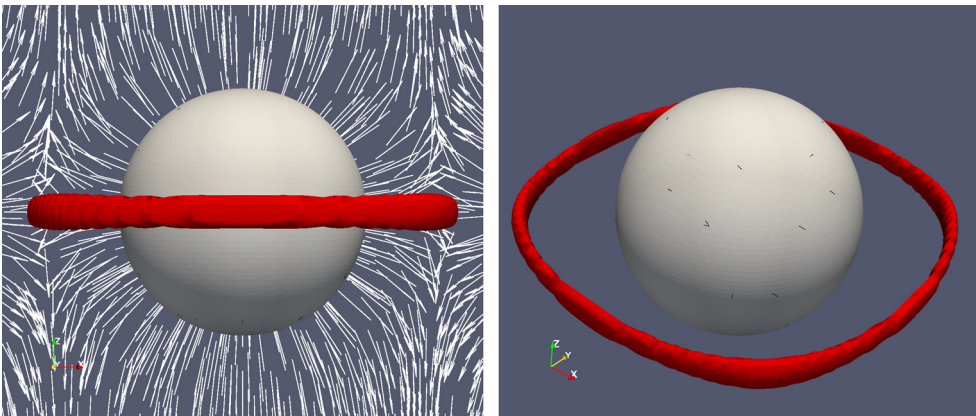

Fig. 16. Simulation results for boundary conditions in (90) ($\kappa = 1.0$) using the immersed boundary approach and anchoring energy (81). The surface mesh of the colloid boundary is shown and the $s = 0.08$ iso-surface is plotted in red which indicates the defect region. The director field is also shown (white arrows) on a plane parallel to the y–z plane and passing through $x = 0.5$. The defect region mimics the classic Saturn ring defect (cf. Section 5.1.3). (For interpretation of the references to color in this figure legend, the reader is referred to the web version of this article.)

6. Electric field

External field effects, such as an electric field, can be modeled by adding another term to the energy. The following sections describe this as well as prove the monotone energy decreasing property of our algorithm applied to the modified energy.

6.1. Modified energy

The energy now takes the form

$$E[s, \mathbf{n}] = E_1[s, \mathbf{n}] + E_2[s] + E_a[s, \mathbf{n}] + E_{\text{ext}}[s, \mathbf{n}],$$ (91)

where $E_{\text{ext}}[s, \mathbf{n}]$ is the external field energy. Following [69,2], we let $E_{\text{ext}}[s, \mathbf{n}]$ be defined by

$$E_{\text{ext}}[s, \mathbf{n}] := -\frac{K_{\text{ext}}}{2} \left(\bar{\varepsilon} \int_{\Omega} (1 - s\gamma_a)|\mathbf{E}|^2 + \varepsilon_a \int_{\Omega} s(\mathbf{E} \cdot \mathbf{n})^2 \right),$$ (92)

where $\mathbf{E}$ is the *given* (fixed) electric field. The other constants are related to the material properties of the liquid crystal medium. Define $\varepsilon_{\parallel}, \varepsilon_{\perp}$ to be the dielectric permittivities in the directions parallel and orthogonal to a liquid crystal molecule. Define $\bar{\varepsilon} = (\varepsilon_{\parallel} + 2\varepsilon_{\perp})/3$ to be the average dielectric permittivity (the 2 is for the two directions orthogonal to the director), $\varepsilon_a = \varepsilon_{\parallel} - \varepsilon_{\perp}$ the dielectric anisotropy, and $\gamma_a = \varepsilon_a/(3\bar{\varepsilon})$ a dimensionless ratio. We allow for ε_a to be positive or negative and note that $0 \le \gamma_a \le 1$ when $0 \le \varepsilon_{\perp} \le \varepsilon_{\parallel}$.

Note that the sign of the second integral in (92) can be negative (however it is bounded because s, $\mathbf{E}$, and $\mathbf{n}$ are bounded). Thus, in order to preserve our energy decreasing minimization scheme (Section 3.2.3), we first introduce a discrete quantity analogous to (76):

$$e_h(s_h, \mathbf{n}_h, \mathbf{v}_h) = \int_{\Omega} I_h \left[|\varepsilon_a||\mathbf{E}|^2 (\mathbf{n}_h \cdot \mathbf{v}_h) - \varepsilon_a s_h (\mathbf{E} \cdot \mathbf{n}_h)(\mathbf{E} \cdot \mathbf{v}_h) \right].$$ (93)

To apply Lemma 6 we see that the matrix H reads

$$H = |\varepsilon_a||\mathbf{E}|^2 \mathbf{I} - \varepsilon_a s_h \mathbf{E} \otimes \mathbf{E},$$

which is symmetric and positive semi-definite because $|s_h| \le 1$. Consequently

$$e_h(s_h, \mathbf{n}_h, \mathbf{n}_h) \ge e_h \left(s_h, \frac{\mathbf{n}_h}{|\mathbf{n}_h|}, \frac{\mathbf{n}_h}{|\mathbf{n}_h|} \right).$$ (94)

We now define the discrete counterpart of (91) to be

$$E^h[s_h, \mathbf{n}_h] := E_1^h[s_h, \mathbf{n}_h] + E_2^h[s_h] + E_a^h[s_h, \mathbf{n}_h] + E_{\text{ext}}^h[s_h, \mathbf{n}_h],$$ (95)

where the discrete electric energy is similar to (92) and is given by

$$E_{\text{ext}}^h[s_h, \mathbf{n}_h] = \frac{K_{\text{ext}}}{2} \left(-\bar{\varepsilon} \int_{\Omega} (1 - s_h\gamma_a)|\mathbf{E}|^2 + e_h(s_h, \mathbf{n}_h, \mathbf{n}_h) - |\varepsilon_a| \int_{\Omega} |\mathbf{E}|^2 \right).$$ (96)

Observe that (96) is an approximation of

$$E_{\text{ext}}^h[s_h, \mathbf{n}_h] = \frac{K_{\text{ext}}}{2} \left(-\bar{\varepsilon} \int_{\Omega} (1 - s_h\gamma_a)|\mathbf{E}|^2 - \varepsilon_a \int_{\Omega} s_h(\mathbf{E} \cdot \mathbf{n}_h)^2 + |\varepsilon_a| \int_{\Omega} |\mathbf{E}|^2 (|\mathbf{n}_h|^2 - 1) \right),$$ (97)

where the "extra" term is non-positive and *consistent* (i.e. it vanishes as $h \to 0$ provided the singular set $\mathbb{S}$ has zero Lebesgue measure). Moreover, $\int_{\Omega} |\mathbf{E}|^2 |\mathbf{n}|^2$ is constant at the continuous level, whence the extra term does not fundamentally change the energy. However, it is needed to ensure the projection step in the algorithm decreases the (discrete) energy, which is guaranteed by (94).
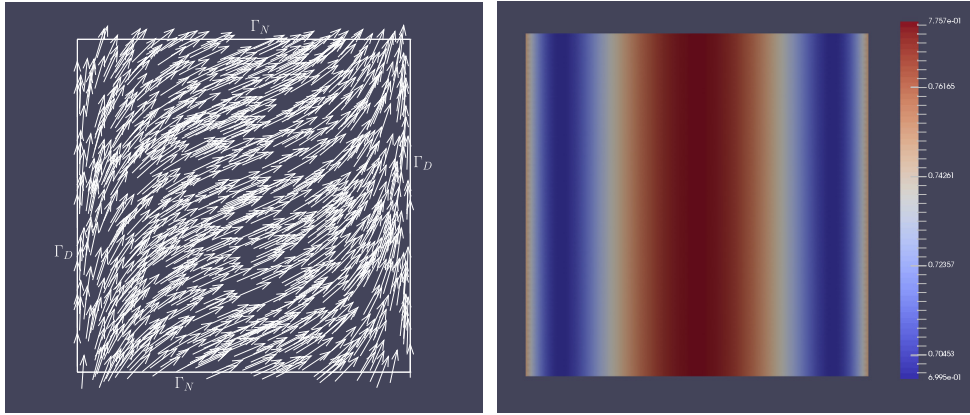
Fig. 17. Simulation results for the Freedericksz transition (Section 6.3.1) with Dirichlet boundary conditions on the left and right of Ω. The director field is shown (white arrows) at equilibrium with the given electric field $\mathbf{E} = (1, 0)^T$. The degree-of-orientation is shown on the right.

6.2. Minimization scheme

We apply the Algorithm of Section 3.2.3 to the energy (95), except we need the following variational derivatives of E_{ext}^h. The first order variation of E_{ext}^h in the direction $\mathbf{v}_h \in \mathbb{U}_h^\perp(\mathbf{n}_h^k) \cap H_{\Gamma_\mathbf{n}}^1(\Omega)$ at the director variable $\mathbf{n}_h^k$ reads

$$\delta_{\mathbf{n}_h} E_{\text{ext}}^h[s_h^k, \mathbf{n}_h^k; \mathbf{v}_h] = K_{\text{ext}} e_h(s_h^k, \mathbf{n}_h^k, \mathbf{v}_h). \tag{98}$$

The first order variation of E_{ext}^h in the direction $z_h \in \mathbb{S}_h \cap H_{\Gamma_s}^1(\Omega)$ at the degree of orientation variable s_h^k is

$$\delta_{s_h} E_{\text{ext}}^h[s_h^k, \mathbf{n}_h^k; z_h] = \frac{K_{\text{ext}}}{2} \left(\bar{\varepsilon} \gamma_a \int_\Omega |\mathbf{E}|^2 z_h - \varepsilon_a \int_\Omega I_h \left[(\mathbf{E} \cdot \mathbf{n}_h^k)^2 z_h \right] \right). \tag{99}$$

6.3. Simulations

We present simulations of the classic Freedericksz transition and the effect of an electric field on the shape of the Saturn ring defect.

6.3.1. Freedericksz transition

We consider a two dimensional cell with no colloids present, i.e. $K_a = 0$. The domain is defined to be $\Omega = [0, 1]^2 \subset \mathbb{R}^2$, with $\Gamma_D = \{0, 1\} \times [0, 1]$, and $\Gamma_N = \partial\Omega \setminus \overline{\Gamma_D}$. The boundary conditions are given by

$$\begin{aligned} \mathbf{n} &= (0, 1)^T, \quad s = s^*, \quad \text{on } \Gamma_D, \\ (\mathbf{\nu} \cdot \nabla)\mathbf{n} &= \mathbf{0}, \quad (\mathbf{\nu} \cdot \nabla)s = 0, \quad \text{on } \Gamma_N, \end{aligned} \tag{100}$$

where $\mathbf{\nu}$ is the outer normal vector of $\partial\Omega$. Moreover, the double well potential is defined in (58). The initial conditions in Ω for the gradient flow are:

$$s = s^*, \qquad \mathbf{n} = (10^{-2}, 1)^T / |(10^{-2}, 1)|.$$

They are chosen to perturb the minimizing pair $\mathbf{n} = (0, 1)^T$, $s = s^*$ without the electric field.

The equilibrium solution, for $\kappa = 1.0$, is shown in Fig. 17, with electric field parameters as follows: $K_{\text{ext}} = 16.0$, $\mathbf{E} = (1, 0)^T$, $\bar{\varepsilon} = 1.0$, $\varepsilon_a = 2.0$, $\gamma_a = 0.5$. The director field deflects toward the right to better align with the imposed electric field $\mathbf{E}$, which is the expected response known as the Freedericksz transition. In this case, $0.6995 \leq s \leq 0.7757$ so the role of s is not so critical because there is no defect region.

6.3.2. Saturn ring interaction with an electric field

We consider the interaction of an electric field with a colloidal particle in three dimensions. The domain is defined to be $\Omega = [0, 1]^3 \subset \mathbb{R}^3$, with $\Gamma_D = \partial\Omega$. The placement of the colloidal sphere and the boundary conditions are the same as in Section 5.2.6 corresponding to Fig. 14, i.e. recall the description in Fig. 11. The double well potential is defined in (58). The weak anchoring parameters are the same as in Section 5.2.6. The electric field parameters are given as follows: $K_{\text{ext}} = 160.0$, $\mathbf{E} = (0, 1, 0)^T$, $\bar{\varepsilon} = 1.0$, $\varepsilon_a = 2.0$, $\gamma_a = 0.5$.

The equilibrium solution, for $\kappa = 1.0$, is shown in Fig. 18. The Saturn ring defect changes significantly (i.e. breaks into four pieces) because K_{ext} is so large. Note that the solution without the electric field is given in Fig. 14.
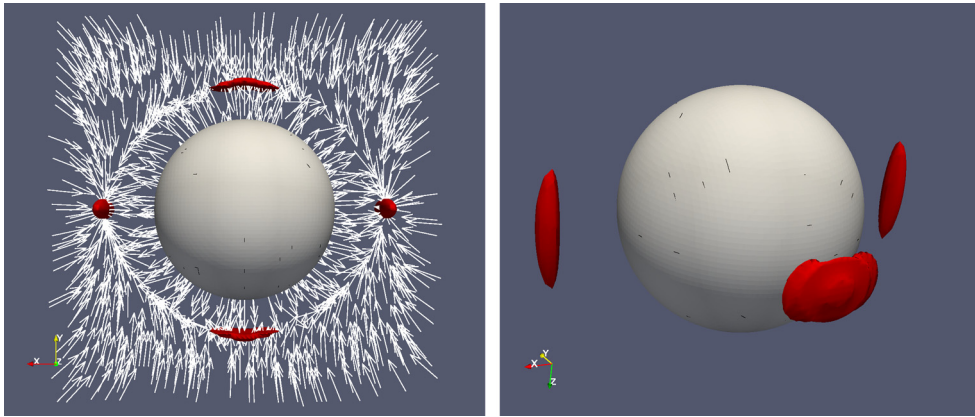
Fig. 18. Simulation results for deforming the Saturn ring with an electric field (Section 6.3.2). The director field is shown (white arrows) at equilibrium with the given electric field $\mathbf{E} = (0, 1, 0)^T$. The $s = 0.15$ iso-surface is shown in red. The ring defect changes into two sliver-like defects and two disk-like defects. The location of the sliver (disk) defect is at a radius of ≈ 0.38 (≈ 0.36); the spherical colloid has a radius of 0.25. (For interpretation of the references to color in this figure legend, the reader is referred to the web version of this article.)

7. Discrete quasi-gradient flow algorithm

We demonstrate that our minimization scheme in Section 3.2.3 monotonically decreases the following discrete total energy

$$E^h[s_h, \mathbf{n}_h] := E_1^h[s_h, \mathbf{n}_h] + E_2^h[s_h] + E_a^h[s_h, \mathbf{n}_h] + E_{\text{ext}}^h[s_h, \mathbf{n}_h], \tag{101}$$

which includes the colloidal and electric field effects.

7.1. Discrete minimizing movements

The method of minimizing movements [90, pg. 32] is rather convenient for ensuring energy decrease even for non-strictly convex energies. Note that this is the case of $\mathbf{n}_h \mapsto E^h[s_h, \mathbf{n}_h]$ for fixed s_h when the latter vanishes at one or more nodes as well as the energies (75) which are degenerate because of the presence of the phase variable ϕ. This approach could be applied to more general non-convex energies as well.

We present the idea for an abstract energy $E : \mathcal{H} \to \mathbb{R}$ where $\mathcal{H}$ is a Hilbert space with norm $\|\cdot\|$ and inner product $\langle \cdot, \cdot \rangle$. We construct a sequence of iterates $\{u^k\}_{n=0}^\infty \subset \mathcal{H}$ as follows: choose $u^0 \in \mathcal{H}$ arbitrarily and consider minimizing the augmented functional

$$F[u] := E[u] + \rho \|u - u^k\|^2$$

for ρ sufficiently large so that F is *strictly convex*. Whether this is possible depends on the specific structure of E, but note that any $\rho > 0$ would work for our two examples in this paper. Let $u^{k+1} \in \mathcal{H}$ be the unique minimizer of F. Then

$$E[u^{k+1}] < F[u^{k+1}] = E[u^k] + \rho \|u^{k+1} - u^k\|^2 \leq F[u^k] = E[u^k], \tag{102}$$

provided $u^{k+1} \neq u^k$. This means that we achieve strict energy decrease unless we reach a stationary point. Convergence of u^k to a local minimizer of E is a delicate matter and within the context of Γ-convergence. We elaborate on both energy decrease and convergence for our concrete functionals below.

7.2. Energy decreasing property

We now capitalize on the preceding calculations to show the following key result, which extends Theorem 3 proved in [61]. Given $(s_h^k, \mathbf{n}_h^k) \in \mathbb{S}_h \times \mathbb{N}_h$, we modify the discrete total energy of (101) as follows for any $\rho \geq 0$:

$$F^h[s_h, \mathbf{n}_h] := E^h[s_h, \mathbf{n}_h] + \rho \|\mathbf{n}_h - \mathbf{n}_h^k\|_{L^2(\Omega)}^2. \tag{103}$$

Theorem 8 (*Energy decrease*). *Let $\mathcal{T}_h$ satisfy* (8). *Given* $(s_h^k, \mathbf{n}_h^k) \in \mathbb{S}_h \times \mathbb{N}_h$, *the iterate* $(s_h^{k+1}, \mathbf{n}_h^{k+1}) \in \mathbb{S}_h \times \mathbb{N}_h$ *of the Algorithm of Section 3.2.3 for* (103) *exists and satisfies*

$$E^h[s_h^{k+1}, \mathbf{n}_h^{k+1}] \leq E^h[s_h^k, \mathbf{n}_h^k] - \frac{1}{\delta t} \int_\Omega (s_h^{k+1} - s_h^k)^2 dx.$$

Equality holds if and only if $(s_h^{k+1}, \mathbf{n}_h^{k+1}) = (s_h^k, \mathbf{n}_h^k)$ *(equilibrium state).*

Proof. Steps (a) and (b) show monotonicity, whereas Step (c) proves strict decrease of the energy.

Step (a): Minimization. Since $F^h[s_h^k, \mathbf{n}_h]$ is convex in $\mathbf{n}_h$ for fixed s_h^k, there exists a tangential variation $\mathbf{t}_h^k$ which minimizes $F^h[s_h^k, \mathbf{n}_h^k + \mathbf{v}_h]$ amongst all tangential variations $\mathbf{v}_h$. Invoking (102) we deduce

$$E^h[s_h^k, \mathbf{n}_h^k + \mathbf{t}_h^k] \le E^h[s_h^k, \mathbf{n}_h^k].$$

Step (b): Projection. Since the mesh $\mathcal{T}_h$ is weakly acute, we claim that

$$\mathbf{n}_h^{k+1} = \frac{\mathbf{n}_h^k + \mathbf{t}_h^k}{|\mathbf{n}_h^k + \mathbf{t}_h^k|} \quad \Rightarrow \quad E^h[s_h^k, \mathbf{n}_h^{k+1}] \le E^h[s_h^k, \mathbf{n}_h^k + \mathbf{t}_h^k].$$

First we show that

$$\mathbf{n}_h^{k+1} = \frac{\mathbf{n}_h^k + \mathbf{t}_h^k}{|\mathbf{n}_h^k + \mathbf{t}_h^k|} \quad \Rightarrow \quad E_1^h[s_h^k, \mathbf{n}_h^{k+1}] \le E_1^h[s_h^k, \mathbf{n}_h^k + \mathbf{t}_h^k].$$

Following [55,91], let $\mathbf{v}_h = \mathbf{n}_h^k + \mathbf{t}_h^k$, $\mathbf{w}_h = \frac{\mathbf{v}_h}{|\mathbf{v}_h|}$, and observe that $|\mathbf{v}_h| \ge 1$ (at the nodes) and $\mathbf{w}_h$ is well-defined. By (14) (definition of the discrete energy), we only need to show that

$$k_{ij} \frac{(s_i^k)^2 + (s_j^k)^2}{2} |\mathbf{w}_h(x_i) - \mathbf{w}_h(x_j)|^2 \le k_{ij} \frac{(s_i^k)^2 + (s_j^k)^2}{2} |\mathbf{v}_h(x_i) - \mathbf{v}_h(x_j)|^2$$

for all $x_i, x_j \in \mathcal{N}_h$. Because $k_{ij} \ge 0$ for $i \ne j$, this is equivalent to showing that $|\mathbf{w}_h(x_i) - \mathbf{w}_h(x_j)| \le |\mathbf{v}_h(x_i) - \mathbf{v}_h(x_j)|$. This follows from the fact that the mapping $\mathbf{a} \mapsto \mathbf{a}/|\mathbf{a}|$ defined on $\{\mathbf{a} \in \mathbb{R}^d : |\mathbf{a}| \ge 1\}$ is Lipschitz continuous with constant 1. Note that equality above holds if and only if $\mathbf{n}_h^{k+1} = \mathbf{n}_h^k$ or equivalently $\mathbf{t}_h^k = \mathbf{0}$.

Next, from (78) and (79), we get

$$E_{\mathrm{a}}^h[s_h^k, \mathbf{n}_h^{k+1}] \le E_{\mathrm{a}}^h[s_h^k, \mathbf{n}_h^k + \mathbf{t}_h^k].$$

Moreover, using (94) and (96), we also get

$$E_{\mathrm{ext}}^h[s_h^k, \mathbf{n}_h^{k+1}] \le E_{\mathrm{ext}}^h[s_h^k, \mathbf{n}_h^k + \mathbf{t}_h^k].$$

Therefore, we find that

$$E^h[s_h^k, \mathbf{n}_h^{k+1}] \le E^h[s_h^k, \mathbf{n}_h^k + \mathbf{t}_h^k].$$

Step (c): Gradient flow. Since E_1^h is quadratic in terms of s_h^k, and

$$2s_h^{k+1}(s_h^{k+1} - s_h^k) = (s_h^{k+1} - s_h^k)^2 + |s_h^{k+1}|^2 - |s_h^k|^2,$$

reordering terms gives

$$E_1^h[s_h^{k+1}, \mathbf{n}_h^{k+1}] - E_1^h[s_h^k, \mathbf{n}_h^{k+1}] = R_1 - E_1^h[s_h^{k+1} - s_h^k, \mathbf{n}_h^{k+1}] \le R_1,$$

where

$$R_1 := \delta_{s_h} E_1^h[s_h^{k+1}, \mathbf{n}_h^{k+1}; s_h^{k+1} - s_h^k].$$

Moreover, E_{a}^h is also quadratic in terms of s_h^k, so we get a similar inequality

$$E_{\mathrm{a}}^h[s_h^{k+1}, \mathbf{n}_h^{k+1}] - E_{\mathrm{a}}^h[s_h^k, \mathbf{n}_h^{k+1}] \le R_{\mathrm{a}},$$

where

$$R_{\mathrm{a}} := \delta_{s_h} E_{\mathrm{a}}^h[s_h^{k+1}, \mathbf{n}_h^{k+1}; s_h^{k+1} - s_h^k].$$

Next, (27) implies

$$E_2^h[s_h^{k+1}] - E_2^h[s_h^k] = \int_\Omega \psi(s_h^{k+1}) dx - \int_\Omega \psi(s_h^k) dx \le R_2 := \delta_{s_h} E_2^h[s_h^{k+1}; s_h^{k+1} - s_h^k],$$

and accounting for the electric field gives

$$E_{\mathrm{ext}}^h[s_h^{k+1}, \mathbf{n}_h^{k+1}] - E_{\mathrm{ext}}^h[s_h^k, \mathbf{n}_h^{k+1}] = R_{\mathrm{ext}} := \delta_{s_h} E_{\mathrm{ext}}^h[s_h^{k+1}, \mathbf{n}_h^{k+1}; s_h^{k+1} - s_h^k].$$

Combining all estimates and invoking Step (c) of the Algorithm yields

$$E^h[s_h^{k+1}, \mathbf{n}_h^{k+1}] - E^h[s_h^k, \mathbf{n}_h^{k+1}] \leq R_1 + R_2 + R_a + R_{\text{ext}} = -\frac{1}{\delta t} \int_\Omega (s_h^{k+1} - s_h^k)^2,$$

which is the assertion. Note finally that equality occurs if and only if $s_h^{k+1} = s_h^k$ and $\mathbf{n}_h^{k+1} = \mathbf{n}_h^k$, which corresponds to an equilibrium state. This completes the proof. □

Remark 9. The choice $\rho > 0$ in (103) ensures a positive definite system to solve for $\mathbf{n}_h^{k+1}$ no matter whether the system for $\rho = 0$ is singular or degenerate (see Remark 5).

8. Γ-convergence of the discrete energy

We show that our discrete energy (101) Γ-converges to the continuous energy

$$E[s, \mathbf{n}] := E_1[s, \mathbf{n}] + E_2[s] + E_a[s, \mathbf{n}] + E_{\text{ext}}[s, \mathbf{n}]. \tag{104}$$

This implies existence of global minimizers of (104), and convergence of global minimizers of (101) to global minimizers of (104) along with convergence of discrete to continuous energies.

We recall the setting of our Γ-convergence result in [61] and next extend it to the more general energy (104). Let the continuous and discrete spaces be

$$\mathbb{X} := L^2(\Omega) \times [L^2(\Omega)]^d, \qquad \mathbb{X}_h := \mathbb{S}_h \times \mathbb{U}_h.$$

We define $E[s, \mathbf{n}]$ as in (104) for $(s, \mathbf{u}) \in \mathbb{A}(g, \mathbf{r})$ and $E[s, \mathbf{u}] = \infty$ for $(s, \mathbf{n}) \in \mathbb{X} \setminus \mathbb{A}(g, \mathbf{r})$. Likewise, we define $E^h[s_h, \mathbf{n}_h]$ as in (101) for $(s_h, \mathbf{u}_h) \in \mathbb{A}_h(g_h, \mathbf{r}_h)$ and $E^h[s, \mathbf{n}] = \infty$ for all $(s, \mathbf{u}) \in \mathbb{X} \setminus \mathbb{A}_h(g_h, \mathbf{r}_h)$. We state the two properties of Γ-convergence for $E_1[s, \mathbf{n}]$ [61].

Theorem 10 (Γ-convergence). *Let $\{\mathcal{T}_h\}$ be a sequence of weakly acute meshes. Then, for every $(s, \mathbf{n}) \in \mathbb{X}$ the following two properties hold:*

- *Lim-inf inequality: for every sequence $\{(s_h, \mathbf{n}_h)\}$ converging strongly to $(s, \mathbf{n})$ in $\mathbb{X}$, we have*

$$E_1[s, \mathbf{n}] \leq \liminf_{h \to 0} E_1^h[s_h, \mathbf{n}_h]; \tag{105}$$

- *Lim-sup inequality: there exists a sequence $\{(s_h, \mathbf{n}_h)\}$ such that $(s_h, \mathbf{n}_h)$ converges strongly to $(s, \mathbf{n})$ in $\mathbb{X}$ and*

$$E_1[s, \mathbf{n}] \geq \limsup_{h \to 0} E_1^h[s_h, \mathbf{n}_h]. \tag{106}$$

We refer to [61] for a complete proof of this rather technical theorem. We now give a brief outline. The lim-sup inequality is a *consistency* estimate in the usual numerical analysis sense. It reduces to showing that $\mathcal{E}_h, \widetilde{\mathcal{E}}_h \to 0$ as $h \to 0$, in (20) and (21). If $\mathbf{n} \in [H^1(\Omega)]^d$, then the residual term (21) would be of order $h^2 \int_\Omega |\nabla s_h|^2 dx$ which obviously converges to zero. The presence of defects entails lack of $[H^1(\Omega)]^d$ regularity of $\mathbf{n}$, whence this heuristic argument fails. A rigorous proof involves a rather delicate regularization argument of any pair $(s, \mathbf{u}) \in \mathbb{A}(g, \mathbf{r})$ which preserves Dirichlet boundary values and the structure condition $\mathbf{u} = s\mathbf{n}$ for some $\mathbf{n}$ of unit norm away from the singular set $\mathbb{S}$.

Proving the lim-inf is more technical. It follows from (19), which also reads

$$E_1^h[s_h, \mathbf{n}_h] \geq (\kappa - 1) \int_\Omega |\nabla I_h|\widetilde{\mathbf{u}}_h||^2 d\mathbf{x} + \int_\Omega |\nabla \widetilde{\mathbf{u}}_h|^2 d\mathbf{x} = \widetilde{E}_1^h[\widetilde{s}_h, \widetilde{\mathbf{u}}_h],$$

and the fact that $\widetilde{E}_1^h[\widetilde{s}_h, \widetilde{\mathbf{u}}_h]$ is weakly lower semi-continuous [61, Lemma 3.4 (weak lower semicontinuity)]. This usually follows from convexity (with respect to $\nabla \widetilde{\mathbf{u}}_h$), but this is **not** obvious when $0 < \kappa < 1$ and is a key contribution of [61].

Γ-convergence combined with a coercivity property yields that global minimizers of the discrete problem converge to global minimizers of the continuous problem [92,93]. We explicitly show this property in Theorem 11. However, Γ-convergence does not yield rates of convergence. In Section 4.6, we provide some experimental rates of convergence.

Theorem 11 (Convergence of global discrete minimizers). *Let $\{\mathcal{T}_h\}$ satisfy (8) and assume E_a, E_a^h are given by (74), (79). If $(s_h, \mathbf{u}_h) \in \mathbb{A}_h(g_h, \mathbf{r}_h)$ is a sequence of global minimizers of $E^h[s_h, \mathbf{n}_h]$ in (101), then every cluster point is a global minimizer of the continuous energy $E[s, \mathbf{n}]$ in (104).*

Proof. We proceed in several steps.

1. *Coercivity*. In view of (101), assume there is a constant $\Lambda > 0$ such that

$$\liminf_{h \to 0} E^h[s_h, \mathbf{n}_h] = \liminf_{h \to 0} \left(E_1^h[s_h, \mathbf{n}_h] + E_2^h[s_h] + E_a^h[s_h, \mathbf{n}_h] + E_{\text{ext}}^h[s_h, \mathbf{n}_h] \right) \le \Lambda,$$

for otherwise there is nothing to prove. We apply [61, Lemma 3.5 (coercivity)]

$$E_1^h[s_h, \mathbf{n}_h] \ge \min\{\kappa, 1\} \int_\Omega |\nabla \widetilde{\mathbf{u}}_h|^2 d\mathbf{x} \ge \min\{\kappa, 1\} \int_\Omega |\nabla I_h|s_h||^2 d\mathbf{x},$$

to extract subsequences (not relabeled) $(\widetilde{s}_h, \widetilde{\mathbf{u}}_h) \to (\widetilde{s}, \widetilde{\mathbf{u}})$ and $(s_h, \mathbf{u}_h) \to (s, \mathbf{u})$ converging weakly in $[H^1(\Omega)]^{d+1}$, strongly in $[L^2(\Omega)]^{d+1}$ and a.e. in Ω. We next invoke [61, Lemma 3.6 (characterizing limits)] to show that the limits satisfy the structure properties

$$\mathbf{u} = s\mathbf{n}, \qquad \widetilde{\mathbf{u}} = \widetilde{s}\mathbf{n} \qquad \text{in } \Omega \setminus \mathbb{S}, \tag{107}$$

for a suitable vector field $\mathbf{n}$, with $|\mathbf{n}| = 1$, and such that $\mathbf{n}_h \to \mathbf{n}$ strongly in $L^2(\Omega \setminus \mathbb{S})$ and a.e. in $\Omega \setminus \mathbb{S}$.

2. *Lim-inf inequality*. Using [61, Lemma 3.4 (weak lower semicontinuity)] we deduce

$$\widetilde{E}_1[\widetilde{s}, \widetilde{\mathbf{u}}] = \int_\Omega (\kappa - 1)|\nabla \widetilde{s}|^2 + |\nabla \widetilde{\mathbf{u}}|^2 d\mathbf{x} \le \liminf_{h \to 0} \widetilde{E}_1^h[\widetilde{s}_h, \widetilde{\mathbf{u}}_h] \le \liminf_{h \to 0} E_1^h[s_h, \mathbf{n}_h],$$

where the last inequality is a consequence of (19). Since s_h converges a.e. in Ω to s, so does $\psi(s_h)$ to $\psi(s)$. Apply now Fatou's lemma to write

$$E_2[s] = \int_\Omega \psi(s) = \int_\Omega \lim_{h \to 0} \psi(s_h) \le \liminf_{h \to 0} \int_\Omega \psi(s_h) = \liminf_{h \to 0} E_2^h[s_h].$$

We now consider the weak anchoring energy $E_a^h[s_h, \mathbf{n}_h]$ of (79), i.e. we show that

$$\int_\Omega s^2 \left[|\mathbf{n}|^2 |\nabla \phi|^2 - (\nabla \phi \cdot \mathbf{n})^2 \right] d\mathbf{x} = \lim_{h \to 0} \int_\Omega I_h \left\{ s_h^2 \left[|\mathbf{n}_h|^2 |\nabla \phi|^2 - (\nabla \phi \cdot \mathbf{n}_h)^2 \right] \right\} d\mathbf{x}. \tag{108}$$

In view of (17), properties of the Lagrange interpolant yield

$$I_h \left\{ s_h^2 \left[|\mathbf{n}_h|^2 |\nabla \phi|^2 - (\nabla \phi \cdot \mathbf{n}_h)^2 \right] \right\} = I_h \left[|\mathbf{u}_h|^2 |\nabla \phi|^2 - (\nabla \phi \cdot \mathbf{u}_h)^2 \right].$$

Next, classic interpolation theory yields

$$\left\| |\mathbf{u}_h|^2 |\nabla \phi|^2 - I_h[|\mathbf{u}_h|^2 |\nabla \phi|^2] \right\|_{L^2(\Omega)} \lesssim h \left\| |\mathbf{u}_h||\nabla \phi|^2 \nabla \mathbf{u}_h \right\|_{L^2(\Omega)} + h \left\| |\mathbf{u}_h|^2 |\nabla \phi| \nabla^2 \phi \right\|_{L^2(\Omega)} \lesssim h \|\mathbf{u}_h\|_{H^1(\Omega)}.$$

Since $\|\mathbf{u}_h\|_{H^1(\Omega)}$ is uniformly bounded, $|\mathbf{u}_h|^2 |\nabla \phi|^2 - I_h[|\mathbf{u}_h|^2 |\nabla \phi|^2] \to 0$ in $L^2(\Omega)$ and a.e. in Ω. Similarly, $(\nabla \phi \cdot \mathbf{u}_h)^2 - I_h[(\nabla \phi \cdot \mathbf{u}_h)^2] \to 0$ in $L^2(\Omega)$ and a.e. in Ω. Hence, using that $\mathbf{u}_h \to \mathbf{u}$ a.e. in Ω and $|\mathbf{u}|$ is uniformly bounded, combining the Lebesgue dominated convergence theorem with (107) implies the following equivalent form of (108)

$$\int_\Omega \left[|\mathbf{u}|^2 |\nabla \phi|^2 - (\nabla \phi \cdot \mathbf{u})^2 \right] d\mathbf{x} = \lim_{h \to 0} \int_\Omega \left[|\mathbf{u}_h|^2 |\nabla \phi|^2 - (\nabla \phi \cdot \mathbf{u}_h)^2 \right] d\mathbf{x}. \tag{109}$$

Furthermore, since ϕ is smooth, the Lebesgue dominated convergence theorem also gives

$$\int_\Omega |\nabla \phi|^2 (s(\mathbf{x}) - s^*)^2 d\mathbf{x} = \lim_{h \to 0} \int_\Omega |I_h \nabla \phi|^2 (s_h(\mathbf{x}) - s^*)^2 d\mathbf{x}.$$

Therefore, we obtain

$$E_a[s, \mathbf{n}] = \lim_{h \to 0} E_a^h[s_h, \mathbf{n}_h]. \tag{110}$$

We proceed similarly for the electric energy (92). In view of (93), (96), we show that

$$\int_\Omega |\varepsilon_a||\mathbf{E}|^2 - \varepsilon_a s(\mathbf{E} \cdot \mathbf{n})^2 d\mathbf{x} = \lim_{h \to 0} \int_\Omega I_h \left[|\varepsilon_a||\mathbf{E}|^2 |\mathbf{n}_h|^2 - \varepsilon_a s_h (\mathbf{E} \cdot \mathbf{n}_h)^2 \right] d\mathbf{x}. \tag{111}$$

First, we exploit that $|\mathbf{n}_h| = 1$ at the nodes to infer that

$$\int_\Omega I_h \left[|\mathbf{E}|^2 |\mathbf{n}_h|^2 \right] = \int_\Omega I_h \left[|\mathbf{E}|^2 \right] \to \int_\Omega |\mathbf{E}|^2, \quad \text{as } h \to 0,$$

because $\mathbf{E}$ is assumed to be smooth. For the other term in (93), nodal interpolation implies

$$I_h \left[s_h (\mathbf{E} \cdot \mathbf{n}_h)^2 \right] = I_h \left[(\mathbf{E} \cdot \mathbf{u}_h)(\mathbf{E} \cdot \mathbf{n}_h) \right],$$

because $\mathbf{u}_h = I_h[s_h \mathbf{n}_h]$. Standard interpolation theory on each element T of $\mathcal{T}_h$ gives

$$\|(\mathbf{E} \cdot \mathbf{u}_h)(\mathbf{E} \cdot \mathbf{n}_h) - I_h[(\mathbf{E} \cdot \mathbf{u}_h)(\mathbf{E} \cdot \mathbf{n}_h)]\|_{L^1(T)} \lesssim h^2 \big(\||\mathbf{u}_h||\mathbf{n}_h|\|_{L^1(T)}$$
$$+ \||\mathbf{u}_h||\nabla \mathbf{n}_h|\|_{L^1(T)} + \||\nabla \mathbf{u}_h||\mathbf{n}_h|\|_{L^1(T)} + \||\nabla \mathbf{u}_h||\nabla \mathbf{n}_h|\|_{L^1(T)} \big).$$

Summing over all $T \in \mathcal{T}_h$, and using Cauchy–Schwarz, we get

$$\|(\mathbf{E} \cdot \mathbf{u}_h)(\mathbf{E} \cdot \mathbf{n}_h) - I_h[(\mathbf{E} \cdot \mathbf{u}_h)(\mathbf{E} \cdot \mathbf{n}_h)]\|_{L^1(\Omega)} \lesssim h^2 \|\mathbf{u}_h\|_{H^1(\Omega)} \|\mathbf{n}_h\|_{H^1(\Omega)}.$$

Since $|\mathbf{n}_h| \leq 1$, an inverse estimate gives $\|\nabla \mathbf{n}_h\|_{L^2(\Omega)} \lesssim h^{-1}$, and so

$$\|(\mathbf{E} \cdot \mathbf{u}_h)(\mathbf{E} \cdot \mathbf{n}_h) - I_h[(\mathbf{E} \cdot \mathbf{u}_h)(\mathbf{E} \cdot \mathbf{n}_h)]\|_{L^1(\Omega)} \lesssim h \|\mathbf{u}_h\|_{H^1(\Omega)} \to 0, \quad \text{as } h \to 0.$$

Thus, we just need to show

$$\int_\Omega (\mathbf{E} \cdot \mathbf{u})(\mathbf{E} \cdot \mathbf{n}) d\mathbf{x} = \lim_{h \to 0} \int_\Omega (\mathbf{E} \cdot \mathbf{u}_h)(\mathbf{E} \cdot \mathbf{n}_h) d\mathbf{x}. \tag{112}$$

We decompose the integral into the singular set $\mathbb{S} = \{s = 0\} = \{\mathbf{u} = \mathbf{0}\}$ and the complement and use the Lebesgue dominated convergence theorem upon realizing that $(\mathbf{E} \cdot \mathbf{u}_h)(\mathbf{E} \cdot \mathbf{n}_h)$ is uniformly bounded. Since $\mathbf{u}_h \to \mathbf{u}$ a.e. in Ω, we obtain

$$\lim_{h \to 0} \int_{\mathbb{S}} (\mathbf{E} \cdot \mathbf{u}_h)(\mathbf{E} \cdot \mathbf{n}_h) d\mathbf{x} = \int_\Omega \chi_{\mathbb{S}} \lim_{h \to 0} (\mathbf{E} \cdot \mathbf{u}_h)(\mathbf{E} \cdot \mathbf{n}_h) d\mathbf{x} = 0.$$

In addition, we utilize [61, Lemma 3.6 (characterizing limits)] to deduce that $\mathbf{n}_h \to \mathbf{n}$ a.e. in $\Omega \setminus \mathbb{S}$, whence

$$\lim_{h \to 0} \int_{\Omega \setminus \mathbb{S}} (\mathbf{E} \cdot \mathbf{u}_h)(\mathbf{E} \cdot \mathbf{n}_h) d\mathbf{x} = \int_{\Omega \setminus \mathbb{S}} (\mathbf{E} \cdot \mathbf{u})(\mathbf{E} \cdot \mathbf{n}) d\mathbf{x}.$$

Collecting the above results, and recalling that $\mathbf{u} = s\mathbf{n}$, we obtain (111). Finally, the Lebesgue dominated convergence theorem implies

$$\int_\Omega (1 - s\gamma_{\mathrm{a}}) |\mathbf{E}|^2 d\mathbf{x} = \lim_{h \to 0} \int_\Omega (1 - s_h \gamma_{\mathrm{a}}) |\mathbf{E}|^2 d\mathbf{x},$$

whence

$$E_{\mathrm{ext}}[s, \mathbf{n}] = \lim_{h \to 0} E_{\mathrm{ext}}^h[s_h, \mathbf{n}_h]. \tag{113}$$

Consequently, we arrived at

$$\widetilde{E}_1[\widetilde{s}, \widetilde{\mathbf{u}}] + E_2[s] + E_{\mathrm{a}}[s, \mathbf{n}] + E_{\mathrm{ext}}[s, \mathbf{n}] \leq \liminf_{h \to 0} E^h[s_h, \mathbf{n}_h]. \tag{114}$$

3. *Lim-sup inequality.* This is a consistency inequality. Since we have to use Lagrange interpolation, and so point values, we first need to invoke a regularization procedure. Given $\epsilon > 0$ arbitrary, we resort to [61, Proposition 3.2 (regularization of functions in $\mathbb{A}_h(g_h, \mathbf{r}_h)$)] to find a pair $(t_\epsilon, \mathbf{v}_\epsilon) \in \mathbb{A}(g, \mathbf{r}) \cap [W^1_\infty(\Omega)]^{d+1}$ such that

$$E[t_\epsilon, \mathbf{m}_\epsilon] \leq \inf_{(t, \mathbf{m}) \in \mathbb{A}(g, \mathbf{r})} E[t, \mathbf{m}] + \epsilon \leq E[s, \mathbf{n}] + \epsilon, \tag{115}$$

where $\mathbf{m}_\epsilon := t_\epsilon^{-1} \mathbf{v}_\epsilon$ if $t_\epsilon \neq 0$ or otherwise $\mathbf{m}_\epsilon$ is an arbitrary unit vector. Let $(t_{\epsilon,h}, \mathbf{v}_{\epsilon,h}) \in \mathbb{A}_h(g_h, \mathbf{r}_h)$ and $\mathbf{m}_{\epsilon,h} \in \mathbb{N}_h$ be the Lagrange interpolants of $(t_\epsilon, \mathbf{v}_\epsilon, \mathbf{m}_\epsilon)$ and apply [61, Lemma 3.3 (lim-sup inequality)] to $(t_\epsilon, \mathbf{v}_\epsilon)$ and $\mathbf{m}_\epsilon$ to write

$$E_1[t_\epsilon, \mathbf{m}_\epsilon] = \lim_{h \to 0} E_1^h[t_{\epsilon,h}, \mathbf{m}_{\epsilon,h}].$$

Moreover, [61, Theorem 3.7 (convergence of global discrete minimizers)] shows that

$$E_2[t_\epsilon] = \int_\Omega \lim_{h \to 0} \psi(t_{\epsilon,h}) = \lim_{h \to 0} \int_\Omega \psi(t_{\epsilon,h}) = \lim_{h \to 0} E_2^h[t_{\epsilon,h}].$$

We now consider the weak anchoring energy (79), and observe that

$$I_h\left\{t_{\epsilon,h}^2\left[|\mathbf{m}_{\epsilon,h}|^2|\nabla\phi|^2 - (\nabla\phi \cdot \mathbf{m}_{\epsilon,h})^2\right]\right\} = I_h\left\{\left[|\mathbf{v}_{\epsilon,h}|^2|\nabla\phi|^2 - (\nabla\phi \cdot \mathbf{v}_{\epsilon,h})^2\right]\right\} \tag{116}$$

because of the definition of Lagrange interpolant and $\mathbf{v}_\epsilon = t_\epsilon \mathbf{m}_\epsilon$. Hence, following a similar argument as in (109), we find that (116) converges in $L^2(\Omega)$ as $h \to 0$ because $\mathbf{v}_\epsilon \in [W_\infty^1(\Omega)]^d$. Therefore, the convergence

$$E_a[t_\epsilon, \mathbf{m}_\epsilon] = \lim_{h \to 0} E_a^h[t_{\epsilon,h}, \mathbf{m}_{\epsilon,h}]$$

follows in a similar fashion as the convergence of (110). Also, since

$$\int_\Omega |I_h\nabla\phi|^2(t_{\epsilon,h} - s^*)^2 \to \int_\Omega |\nabla\phi|^2(t_\epsilon - s^*)^2, \quad \text{as } h \to 0, \tag{117}$$

by standard interpolation theory, taking (116) and (117) together, we get

$$E_a[t_\epsilon, \mathbf{m}_\epsilon] = \lim_{h \to 0} E_a^h[t_{\epsilon,h}, \mathbf{m}_{\epsilon,h}].$$

For the electric energy (96), the definition of the Lagrange interpolant again implies

$$I_h\left[|\varepsilon_a||\mathbf{E}|^2|\mathbf{m}_{\epsilon,h}|^2 - \varepsilon_a t_{\epsilon,h}(\mathbf{E} \cdot \mathbf{m}_{\epsilon,h})^2\right] = I_h\left[|\varepsilon_a||\mathbf{E}|^2 - \varepsilon_a t_\epsilon(\mathbf{E} \cdot \mathbf{m}_\epsilon)^2\right]. \tag{118}$$

The first term in (118) clearly converges to $|\varepsilon_a||\mathbf{E}|^2$ in $L^1(\Omega)$. For the second term $\xi_\epsilon := t_\epsilon(\mathbf{E} \cdot \mathbf{m}_\epsilon)^2$, take $\delta > 0$ arbitrary, define $\mathbb{S}_\delta := \{|t_\epsilon| \le \delta\}$, and note that

$$x_i \in \mathcal{N}_h: \quad |x - x_i| \le Ch \quad \Rightarrow \quad |t_\epsilon(x) - t_\epsilon(x_i)| \le C_\epsilon h.$$

Let h be small, depending on ϵ and δ, so that $C_\epsilon h \le \frac{\delta}{2}$. If $x \in \mathbb{S}_\delta$, then $t_\epsilon(x_i) \le \frac{3}{2}\delta$ and

$$\int_{\mathbb{S}_\delta} |\xi_\epsilon - I_h\xi_\epsilon| \le C_\epsilon\delta.$$

On the other hand, if $x \notin \mathbb{S}_\delta$, then $t_\epsilon(x_i) \ge \frac{1}{2}\delta$ and ξ_ϵ is Lipschitz in $\Omega \setminus \mathbb{S}_{\frac{\delta}{2}}$ with constant $C_{\epsilon,\delta}$. Therefore

$$\int_{\Omega\setminus\mathbb{S}_\delta} |\xi_\epsilon - I_h\xi_\epsilon| \le C_{\epsilon,\delta}h.$$

Taking the limits, first as $h \to 0$ and next as $\delta \to 0$, we infer that

$$\lim_{h \to 0} \int_\Omega I_h\xi_\epsilon dx = \int_\Omega \xi_\epsilon dx$$

which implies convergence of the second term in (118). Moreover, since $\int_\Omega t_{\epsilon,h}|\mathbf{E}|^2 dx \to \int_\Omega t_\epsilon|\mathbf{E}|^2 dx$, as $h \to 0$, we obtain

$$E_{\text{ext}}[t_\epsilon, \mathbf{m}_\epsilon] = \lim_{h \to 0} E_{\text{ext}}^h[t_{\epsilon,h}, \mathbf{m}_{\epsilon,h}].$$

Collecting the preceding estimates we end up with the lim-sup equality

$$E[t_\epsilon, \mathbf{v}_\epsilon] = \lim_{h \to 0} E^h[t_{\epsilon,h}, \mathbf{v}_{\epsilon,h}]. \tag{119}$$

4. *Convergence of energy.* We observe that $\nabla\widetilde{\mathbf{u}} = \nabla\widetilde{s} \otimes \mathbf{n} + \widetilde{s}\nabla\mathbf{n}$ a.e. in $\Omega \setminus \mathbb{S}$, whence

$$\widetilde{E}_1[\widetilde{s}, \widetilde{\mathbf{u}}] = \int_{\Omega\setminus\mathbb{S}} \kappa|\nabla\widetilde{s}|^2 + |\widetilde{s}|^2|\nabla\mathbf{n}|^2 = \int_{\Omega\setminus\mathbb{S}} \kappa|\nabla s|^2 + |s|^2|\nabla\mathbf{n}|^2 = E_1[s, \mathbf{n}],$$

and note that $\Omega \setminus \mathbb{S}$ can be replaced by Ω because $\nabla s = \mathbf{0}$ on $\mathbb{S}$. Therefore, in view of (114), (115) and (119), we arrive at

$$E[s, \mathbf{n}] \leq \liminf_{h \to 0} E^h[s_h, \mathbf{n}_h] \leq \limsup_{h \to 0} E^h[s_h, \mathbf{n}_h] \leq \lim_{h \to 0} E^h[t_{\epsilon,h}, \mathbf{n}_{\epsilon,h}] = E[t_\epsilon, \mathbf{v}_\epsilon] \leq E[s, \mathbf{n}] + \epsilon.$$

Finally, letting $\epsilon \to 0$, we see that the pair $(s, \mathbf{n})$ is a global minimizer of E and $E[s, \mathbf{n}] = \lim_{h \to 0} E^h[s_h, \mathbf{n}_h]$, as asserted. This concludes the proof. $\square$

It remains to show the Γ-convergence when the discrete weak anchoring energy (79) is replaced by the penalized Dirichlet energy (81).

Corollary 12 (*Convergence of global discrete minimizers*). *Let* $\{\mathcal{T}_h\}$ *satisfy* (8) *and assume* E_a, E_a^h *are given by* (80), (81). *If* $(s_h, \mathbf{u}_h) \in \mathbb{A}_h(g_h, \mathbf{r}_h)$ *is a sequence of global minimizers of* $E^h[s_h, \mathbf{n}_h]$ *in* (101), *then every cluster point is a global minimizer of the continuous energy* $E[s, \mathbf{n}]$ *in* (104).

Proof. Following the proof of Theorem 11, we only need to show that the lim-inf and lim-sup inequalities hold for the anchoring energy (81).

Step 1. Lim-inf inequality: Thanks to Step 1 in Theorem 11, any $(s_h, \mathbf{u}_h) \to (s, \mathbf{u})$ converging in $\mathbb{X}$, there exists a subsequence $(s_h, \mathbf{u}_h) \to (s, \mathbf{u})$ converging weakly in $[H^1(\Omega)]^{d+1}$, strongly in $[L^2(\Omega)]^{d+1}$ and a.e. in Ω. To prove the limit-inf equality, we note that

$$E_a^h[s_h, \mathbf{n}_h] = \frac{K_a}{2} C_0 \epsilon \left(\int_\Omega I_h \left\{ s_h^2 ||\nabla\phi|\mathbf{n}_h - \nabla\phi|^2 \right\} + \int_\Omega |I_h \nabla\phi|^2 (s_h - g_h)^2 \right)$$

$$= \frac{K_a}{2} C_0 \epsilon \left(\int_\Omega I_h \left\{ |T_1^h|^2 \right\} + \int_\Omega (T_2^h)^2 \right),$$

where

$$T_1^h := |\nabla\phi|\mathbf{u}_h - s_h \nabla\phi \quad \text{and} \quad T_2^h := |I_h \nabla\phi|(s_h - g_h).$$

For the first term T_1^h, since $\mathbf{u}_h$ and s_h converge to $\mathbf{u}$ and s in $L^2(\Omega)$, we note that

$$T_1^h \to T_1 := |\nabla\phi|\mathbf{u} - s\nabla\phi \quad \text{in } L^2(\Omega) \text{ as } h \to 0.$$

Therefore, $\int_\Omega (T_1^h)^2 \to \int_\Omega (T_1)^2$ which implies that (similar to what is done in (109))

$$\int_\Omega I_h\{(T_1^h)^2 - (T_1)^2\} \leq C \int_\Omega (T_1^h)^2 - (T_1)^2 \to 0 \quad \text{as } h \to 0.$$

Moreover, since $\int_\Omega I_h\{(T_1)^2\} \to \int_\Omega (T_1)^2$ as $h \to 0$, we obtain that

$$\int_\Omega I_h \left\{ (T_1^h)^2 \right\} \to \int_\Omega (T_1)^2. \tag{120}$$

For the second term T_2^h, we have

$$T_2^h \to T_2 := |\nabla\phi|(s - g) \quad \text{a.e. as } h \to 0 \quad \text{and} \quad |T_2^h| \leq 2 \max_\Omega |\nabla\phi|.$$

By the Lebesgue dominated convergence theorem, we have

$$\int_\Omega (T_2^h)^2 \to \int_\Omega (T_2)^2.$$

Combining this with (120), we infer that

$$\lim_{h \to 0} E_a^h[s_h, \mathbf{u}_h] = E_a[s, \mathbf{u}].$$

Step 2. Lim-sup inequality: We follow step 3 in the proof of Theorem 11 and set $(t_\epsilon, \mathbf{v}_\epsilon) \in \mathbb{A}(g, \mathbf{r}) \cap [W_\infty^1(\Omega)]^{d+1}$ such that $(t_\epsilon, \mathbf{v}_\epsilon) \to (s, \mathbf{u})$ weakly in $[H^1(\Omega)]^{d+1}$, strongly in $[L^2(\Omega)]^{d+1}$ and a.e. in Ω. Let $(t_{\epsilon,h}, \mathbf{v}_{\epsilon,h})$ be the Lagrange interpolants

of $(t_\epsilon, \mathbf{v}_\epsilon)$, then $(t_{\epsilon,h}, \mathbf{v}_{\epsilon,h}) \to (t_\epsilon, \mathbf{v}_\epsilon)$ strongly in $[L^2(\Omega)]^{d+1}$ and a.e. in Ω. By a similar procedure as before, we are able to show that

$$\lim_{h \to 0} E_a^h[t_{\epsilon,h}, \mathbf{v}_{\epsilon,h}] = E_a[t_\epsilon, \mathbf{v}_\epsilon].$$

This concludes the proof. $\square$

9. Conclusions

We present a robust finite element method for the Ericksen energy that models nematic liquid crystals with variable degree of orientation. This is augmented by additional energy terms to model colloidal effects and electric fields. We present several simulations to illustrate the diverse range of phenomena that can be captured by our method, e.g. interesting defect structures (such as the Saturn ring) as well as the ability to modulate the defect structures with external fields. We prove a monotone energy decreasing property for our quasi-gradient flow method (applied to (101)) which hinges on a mass-lumping strategy for the auxiliary energy terms E_a^h and E_{ext}^h. Furthermore, we provide a full Γ-convergence proof of our discrete energy (101) to the original continuous energy (104).

The following are possible extensions of this work: modeling of liquid crystal droplets, i.e. by coupling the Ericksen energy to Cahn–Hilliard; coupling with full electro-statics with or without charge transport, as well as including electro-dynamics to model liquid crystal laser devices; and also optimizing colloidal particle distributions by actuating the liquid crystal medium. Furthermore, we plan on extending our method to handle the full **Q**-tensor model.

References

[1] J. Ericksen, Liquid crystals with variable degree of orientation, Arch. Ration. Mech. Anal. 113 (2) (1991) 97–120, http://dx.doi.org/10.1007/BF00380413.
[2] P.G. de Gennes, J. Prost, The Physics of Liquid Crystals, 2nd edition, International Series of Monographs on Physics, vol. 83, Oxford Science Publication, Oxford, UK, 1995.
[3] J.W. Goodby, Introduction to defect textures in liquid crystals, in: Janglin Chen, Wayne Cranton, Mark Fihn (Eds.), Handbook of Visual Display Technology, Springer, 2012, pp. 1290–1314.
[4] R. Perkins, Liquid crystal, http://www.teachersource.com/downloads/lesson_pdf/LC-AST.pdf, 2009.
[5] B. Senyuk, Liquid crystals: a simple view on a complex matter, http://www.personal.kent.edu/bisenyuk/liquidcrystals/, 2010.
[6] P.J. Ackerman, J. van de Lagemaat, I.I. Smalyukh, Self-assembly and electrostriction of arrays and chains of hopfion particles in chiral liquid crystals, Nat. Commun. 6 (2015), http://dx.doi.org/10.1038/ncomms7012.
[7] T. Araki, H. Tanaka, Colloidal aggregation in a nematic liquid crystal: topological arrest of particles by a single-stroke disclination line, Phys. Rev. Lett. 97 (2006) 127801, http://dx.doi.org/10.1103/PhysRevLett.97.127801.
[8] H.K. Bisoyi, S. Kumar, Liquid-crystal nanoscience: an emerging avenue of soft self-assembly, Chem. Soc. Rev. 40 (2011) 306–319, http://dx.doi.org/10.1039/B901793N.
[9] C. Blanc, Colloidal crystal ordering in a liquid crystal, Science 352 (6281) (2016) 40–41, http://dx.doi.org/10.1126/science.aaf4260, http://science.sciencemag.org/content/352/6281/40.
[10] L. Blinov, Electro-Optical and Magneto-Optical Properties of Liquid Crystals, Wiley, 1983.
[11] H. Coles, S. Morris, Liquid–crystal lasers, Nat. Photonics 4 (10) (2010) 676–685.
[12] M. Conradi, M. Ravnik, M. Bele, M. Zorko, S. Žumer, I. Muševič, Janus nematic colloids, Soft Matter 5 (2009) 3905–3912, http://dx.doi.org/10.1039/B905631A.
[13] M. Hain, R. Glöckner, S. Bhattacharya, D. Dias, S. Stankovic, T. Tschudi, Fast switching liquid crystal lenses for a dual focus digital versatile disc pickup, Opt. Commun. 188 (5–6) (2001) 291–299, http://dx.doi.org/10.1016/S0030-4018(01)00989-0, http://www.sciencedirect.com/science/article/pii/S0030401801009890.
[14] M. Humar, I. Muševič, 3d microlasers from self-assembled cholesteric liquid–crystal microdroplets, Opt. Express 18 (26) (2010) 26995–27003, http://dx.doi.org/10.1364/OE.18.026995, http://www.opticsexpress.org/abstract.cfm?URI=oe-18-26-26995.
[15] J.A. Moreno-Razo, E.J. Sambriski, N.L. Abbott, J.P. Hernández-Ortiz, J.J. de Pablo, Liquid–crystal-mediated self-assembly at nanodroplet interfaces, Nature 485 (7396) (2012) 86–89, http://dx.doi.org/10.1038/nature11084.
[16] I. Muševič, M. Škarabot, U. Tkalec, M. Ravnik, S. Žumer, Two-dimensional nematic colloidal crystals self-assembled by topological defects, Science 313 (5789) (2006) 954–958, http://dx.doi.org/10.1126/science.1129660, http://www.sciencemag.org/content/313/5789/954.abstract.
[17] I. Muševič, S. Žumer, Liquid crystals: maximizing memory, Nat. Mater. 10 (4) (2011) 266–268.
[18] M. Rahimi, T.F. Roberts, J.C. Armas-Pérez, X. Wang, E. Bukusoglu, N.L. Abbott, J.J. de Pablo, Nanoparticle self-assembly at the interface of liquid crystal droplets, Proc. Natl. Acad. Sci. USA 112 (17) (2015) 5297–5302, http://dx.doi.org/10.1073/pnas.1422785112, http://www.pnas.org/content/112/17/5297.abstract.
[19] A.A. Shah, H. Kang, K.L. Kohlstedt, K.H. Ahn, S.C. Glotzer, C.W. Monroe, M.J. Solomon, Self-assembly: liquid crystal order in colloidal suspensions of spheroidal particles by direct current electric field assembly (small 10/2012), Small 8 (10) (2012) 1457, http://dx.doi.org/10.1002/smll.201290056.
[20] J. Sun, H. Wang, L. Wang, H. Cao, H. Xie, X. Luo, J. Xiao, H. Ding, Z. Yang, H. Yang, Preparation and thermo-optical characteristics of a smart polymer-stabilized liquid crystal thin film based on smectic A–chiral nematic phase transition, Smart Mater. Struct. 23 (12) (2014) 125038, http://stacks.iop.org/0964-1726/23/i=12/a=125038.

[21] M. Wang, L. He, S. Zorba, Y. Yin, Magnetically actuated liquid crystals, Nano Lett. 14 (7) (2014) 3966–3971, https://doi.org/10.1021/nl501302s, pMID: 24914876.

[22] S. Čopar, M. Ravnik, S. Žumer, Janus nematic colloids with designable valence, Materials 7 (6) (2014) 4272, http://dx.doi.org/10.3390/ma7064272, http://www.mdpi.com/1996-1944/7/6/4272.

[23] Z. Eskandari, N.M. Silvestre, M.M. Telo da Gama, Bonded boojum-colloids in nematic liquid crystals, Langmuir 29 (33) (2013) 10360–10367, http://dx.doi.org/10.1021/la4017195, pMID: 23859624.

[24] E.M. Furst, Directing colloidal assembly at fluid interfaces, Proc. Natl. Acad. Sci. USA 108 (52) (2011) 20853–20854, http://dx.doi.org/10.1073/pnas.1118441109, http://www.pnas.org/content/108/52/20853.full.pdf+html, http://www.pnas.org/content/108/52/20853.short.

[25] I.W. Hamley, Nanotechnology with soft materials, Angew. Chem., Int. Ed. 42 (15) (2003) 1692–1712, http://dx.doi.org/10.1002/anie.200200546.

[26] P.C. Hiemenz, R. Rajagopalan, Principles of Colloid and Surface Chemistry, 3rd edition, Marcel Dekker, Inc., New York, Basel, Hong Kong, 1997.

[27] J. Jeong, A. Gross, W.-S. Wei, F. Tu, D. Lee, P. Collings, A. Yodh, Liquid crystal Janus emulsion droplets: preparation, tumbling, and swimming, Soft Matter (2015), http://dx.doi.org/10.1039/C5SM01053E.

[28] O.V. Kuksenok, R.W. Ruhwandl, S.V. Shiyanovskii, E.M. Terentjev, Director structure around a colloid particle suspended in a nematic liquid crystal, Phys. Rev. E 54 (1996) 5198–5203, http://dx.doi.org/10.1103/PhysRevE.54.5198.

[29] Q. Liu, B. Senyuk, M. Tasinkevych, I.I. Smalyukh, Nematic liquid crystal boojums with handles on colloidal handlebodies, Proc. Natl. Acad. Sci. USA 110 (23) (2013) 9231–9236, http://dx.doi.org/10.1073/pnas.1301464110, http://www.pnas.org/content/110/23/9231.full.pdf, http://www.pnas.org/content/110/23/9231.abstract.

[30] M. Tasinkevych, N.M. Silvestre, M.M.T. da Gama, Liquid crystal boojum-colloids, New J. Phys. 14 (7) (2012) 073030, http://stacks.iop.org/1367-2630/14/i=7/a=073030.

[31] Y. Wang, Y. Wang, D.R. Breed, V.N. Manoharan, L. Feng, A.D. Hollingsworth, M. Weck, D.J. Pine, Colloids with valence and specific directional bonding, Nature 491 (7422) (2012) 51–55.

[32] E.G. Virga, Variational Theories for Liquid Crystals, vol. 8, 1st edition, Chapman and Hall, London, 1994.

[33] M. Calderer, D. Golovaty, F. Lin, C. Liu, Time evolution of nematic liquid crystals with variable degree of orientation, SIAM J. Math. Anal. 33 (5) (2002) 1033–1047, http://dx.doi.org/10.1137/S0036141099362086, http://epubs.siam.org/doi/pdf/10.1137/S0036141099362086.

[34] L. Ambrosio, Regularity of solutions of a degenerate elliptic variational problem, Manuscr. Math. 68 (1) (1990) 309–326, http://dx.doi.org/10.1007/BF02568766.

[35] L. Ambrosio, Existence of minimal energy configurations of nematic liquid crystals with variable degree of orientation, Manuscr. Math. 68 (1) (1990) 215–228, http://dx.doi.org/10.1007/BF02568761.

[36] P. Bauman, M.C. Calderer, C. Liu, D. Phillips, The phase transition between chiral nematic and smectic a* liquid crystals, Arch. Ration. Mech. Anal. 165 (2) (2002) 161–186, http://dx.doi.org/10.1007/s00205-002-0223-8.

[37] J.M. Ball, A. Zarnescu, Orientability and energy minimization in liquid crystal models, Arch. Ration. Mech. Anal. 202 (2) (2011) 493–535, http://dx.doi.org/10.1007/s00205-011-0421-3.

[38] F.-H. Lin, Nonlinear theory of defects in nematic liquid crystals; phase transition and flow phenomena, Commun. Pure Appl. Math. 42 (6) (1989) 789–814, http://dx.doi.org/10.1002/cpa.3160420605.

[39] F.H. Lin, On nematic liquid crystals with variable degree of orientation, Commun. Pure Appl. Math. 44 (4) (1991) 453–468, http://dx.doi.org/10.1002/cpa.3160440404.

[40] J.M. Ball, A. Zarnescu, Orientable and non-orientable director fields for liquid crystals, Proc. Appl. Math. Mech. 7 (1) (2007) 1050701–1050704, http://dx.doi.org/10.1002/pamm.200700489.

[41] D. Golovaty, L.K. Gross, S.I. Hariharan, E.C. Gartland Jr., On instability of a bend Fréedericksz configuration in nematic liquid crystals, J. Math. Anal. Appl. 255 (2) (2001) 391–403, http://dx.doi.org/10.1006/jmaa.2000.7129, http://www.sciencedirect.com/science/article/pii/S0022247X00971294.

[42] R. Hardt, D. Kinderlehrer, F.-H. Lin, Stable defects of minimizers of constrained variational principles, Ann. Inst. Henri Poincaré (C), Anal. Non Linéaire 5 (4) (1988) 297–322, http://eudml.org/doc/78155.

[43] R. Hardt, D. Kinderlehrer, M. Luskin, Remarks about the mathematical theory of liquid crystals, in: S. Hildebrandt, D. Kinderlehrer, M. Miranda (Eds.), Calculus of Variations and Partial Differential Equations, in: Lecture Notes in Mathematics, vol. 1340, Springer, Berlin, Heidelberg, 1988, pp. 123–138.

[44] F.-H. Lin, C. Liu, Static and dynamic theories of liquid crystals, J. Partial Differ. Equ. 14 (4) (2001) 289–330.

[45] S. Badia, F.M. Guillén-González, J.V. Gutiérrez-Santacreu, An overview on numerical analyses of nematic liquid crystal flows, Arch. Comput. Methods Eng. 18 (3) (2011) 285–313, http://dx.doi.org/10.1007/s11831-011-9061-x.

[46] J.W. Barrett, X. Feng, A. Prohl, Convergence of a fully discrete finite element method for a degenerate parabolic system modelling nematic liquid crystals with variable degree of orientation, ESAIM: Math. Model. Numer. Anal. 40 (2006) 175–199, http://dx.doi.org/10.1051/m2an:2006005, http://www.esaim-m2an.org/article_S0764583X06000057.

[47] P.A. Cruz, M.F. Tomé, I.W. Stewart, S. McKee, Numerical solution of the Ericksen–Leslie dynamic equations for two-dimensional nematic liquid crystal flows, J. Comput. Phys. 247 (2013) 109–136, http://dx.doi.org/10.1016/j.jcp.2013.03.061, http://www.sciencedirect.com/science/article/pii/S0021999113002453.

[48] A. Ramage, E.C. Gartland Jr., A preconditioned nullspace method for liquid crystal director modeling, SIAM J. Sci. Comput. 35 (1) (2013) B226–B247, http://dx.doi.org/10.1137/120870219.

[49] J.H. Adler, T.J. Atherton, T.R. Benson, D.B. Emerson, S.P. MacLachlan, Energy minimization for liquid crystal equilibrium with electric and flexoelectric effects, SIAM J. Sci. Comput. 37 (5) (2015) S157–S176, http://dx.doi.org/10.1137/140975036.

[50] J.H. Adler, T.J. Atherton, D.B. Emerson, S.P. MacLachlan, An energy-minimization finite-element approach for the Frank–Oseen model of nematic liquid crystals, SIAM J. Numer. Anal. 53 (5) (2015) 2226–2254, http://dx.doi.org/10.1137/140956567.

[51] J.H. Adler, D.B. Emerson, S.P. MacLachlan, T.A. Manteuffel, Constrained optimization for liquid crystal equilibria, SIAM J. Sci. Comput. 38 (1) (2016) B50–B76, http://dx.doi.org/10.1137/141001846.

[52] S. Bartels, Numerical analysis of a finite element scheme for the approximation of harmonic maps into surfaces, Math. Comput. 79 (271) (2010) 1263–1301.

[53] R. Cohen, S.-Y. Lin, M. Luskin, Relaxation and gradient methods for molecular orientation in liquid crystals, Comput. Phys. Commun. 53 (13) (1989) 455–465, http://dx.doi.org/10.1016/0010-4655(89)90178-1, http://www.sciencedirect.com/science/article/pii/0010465589901781.

[54] S.-Y. Lin, M. Luskin, Relaxation methods for liquid crystal problems, SIAM J. Numer. Anal. 26 (6) (1989) 1310–1324, http://www.jstor.org/stable/2157741.

[55] F. Alouges, A new algorithm for computing liquid crystal stable configurations: the harmonic mapping case, SIAM J. Numer. Anal. 34 (5) (1997) 1708–1726, http://www.jstor.org/stable/2952012.

[56] F.M.G. González, J.V. Gutiérrez-Santacreu, A linear mixed finite element scheme for a nematic Ericksen–Leslie liquid crystal model, ESAIM: Math. Model. Numer. Anal. 47 (2013) 1433–1464, http://dx.doi.org/10.1051/m2an/2013076, http://www.esaim-m2an.org/article_S0764583X13000769.

[57] C. Liu, N. Walkington, Approximation of liquid crystal flows, SIAM J. Numer. Anal. 37 (3) (2000) 725–741, http://dx.doi.org/10.1137/S0036142997327282, http://epubs.siam.org/doi/pdf/10.1137/S0036142997327282.

[58] N.J. Walkington, Numerical approximation of nematic liquid crystal flows governed by the Ericksen–Leslie equations, ESAIM: Math. Model. Numer. Anal. 45 (2011) 523–540, http://dx.doi.org/10.1051/m2an/2010065, http://www.esaim-m2an.org/article_S0764583X10000658.

[59] X. Yang, M.G. Forest, C. Liu, J. Shen, Shear cell rupture of nematic liquid crystal droplets in viscous fluids, J. Non-Newton. Fluid Mech. 166 (9–10) (2011) 487–499, http://dx.doi.org/10.1016/j.jnnfm.2011.02.004, http://www.sciencedirect.com/science/article/pii/S0377025711000450.

[60] X. Yang, M.G. Forest, H. Li, C. Liu, J. Shen, Q. Wang, F. Chen, Modeling and simulations of drop pinch-off from liquid crystal filaments and the leaky liquid crystal faucet immersed in viscous fluids, J. Comput. Phys. 236 (2013) 1–14, http://dx.doi.org/10.1016/j.jcp.2012.10.042, http://www.sciencedirect.com/science/article/pii/S0021999112006456.

[61] R.H. Nochetto, S.W. Walker, W. Zhang, A finite element method for nematic liquid crystals with variable degree of orientation, SIAM J. Numer. Anal. 55 (2017) 1357–1386.

[62] R.H. Nochetto, S.W. Walker, W. Zhang, Numerics for liquid crystals with variable degree of orientation, in: Symposium NN – Mathematical and Computational Aspects of Materials Science, in: MRS Proceedings, vol. 1753, 2015, http://journals.cambridge.org/article_S1946427415001591.

[63] F. Bethuel, H. Brezis, F. Hélein, Ginzburg–Landau Vortices, Progress in Nonlinear Differential Equations and Their Applications, vol. 13, Birkhäuser Boston Inc., Boston, MA, 1994.

[64] H. Brezis, J.-M. Coron, E.H. Lieb, Harmonic maps with defects, Commun. Math. Phys. 107 (4) (1986) 649–705, http://dx.doi.org/10.1007/BF01205490.

[65] R. Schoen, K. Uhlenbeck, A regularity theory for harmonic maps, J. Differ. Geom. 17 (2) (1982) 307–335.

[66] K. Tojo, A. Furukawa, T. Araki, A. Onuki, Defect structures in nematic liquid crystals around charged particles, Eur. Phys. J. E 30 (1) (2009) 55–64, http://dx.doi.org/10.1140/epje/i2009-10506-7.

[67] A. Braides, Gamma-Convergence for Beginners, Oxford Lecture Series in Mathematics and Its Applications, vol. 22, Oxford Scholarship, 2002.

[68] Y. Gu, N.L. Abbott, Observation of Saturn-ring defects around solid microspheres in nematic liquid crystals, Phys. Rev. Lett. 85 (2000) 4719–4722, http://dx.doi.org/10.1103/PhysRevLett.85.4719.

[69] P. Biscari, P. Cesana, Ordering effects in electric splay Freedericksz transitions, Contin. Mech. Thermodyn. 19 (5) (2007) 285–298, http://dx.doi.org/10.1007/s00161-007-0055-8.

[70] J. Hoogboom, J.A. Elemans, A.E. Rowan, T.H. Rasing, R.J. Nolte, The development of self-assembled liquid crystal display alignment layers, Philos. Trans. R. Soc. Lond. A, Math. Phys. Eng. Sci. 365 (1855) (2007) 1553–1576, http://dx.doi.org/10.1098/rsta.2007.2031.

[71] P. Ciarlet, P.-A. Raviart, Maximum principle and uniform convergence for the finite element method, Comput. Methods Appl. Mech. Eng. 2 (1) (1973) 17–31, http://dx.doi.org/10.1016/0045-7825(73)90019-4, http://www.sciencedirect.com/science/article/pii/0045782573900194.

[72] G. Strang, G. Fix, An Analysis of the Finite Element Method, 2nd edition, Wellesley-Cambridge, 2008.

[73] S. Korotov, M. Křížek, P. Neittaanmäkia, Weakened acute type condition for tetrahedral triangulations and the discrete maximum principle, Math. Comput. 70 (233) (2001) 107–119, http://dx.doi.org/10.1090/S0025-5718-00-01270-9.

[74] J.H. Brandts, S. Korotov, M. Křížek, The discrete maximum principle for linear simplicial finite element approximations of a reaction–diffusion problem, Linear Algebra Appl. 429 (10) (2008) 2344–2357, http://dx.doi.org/10.1016/j.laa.2008.06.011, special Issue in honor of Richard S. Varga, http://www.sciencedirect.com/science/article/pii/S0024379508003054.

[75] S.M. Wise, C. Wang, J.S. Lowengrub, An energy-stable and convergent finite-difference scheme for the phase field crystal equation, SIAM J. Numer. Anal. 47 (3) (2009) 2269–2288, http://dx.doi.org/10.1137/080738143.

[76] J. Shen, X. Yang, Numerical approximations of Allen–Cahn and Cahn–Hilliard equations, Discrete Contin. Dyn. Syst. 28 (4) (2010) 1669–1691.

[77] J. Shen, X. Yang, A phase-field model and its numerical approximation for two-phase incompressible flows with different densities and viscosities, SIAM J. Sci. Comput. 32 (3) (2010) 1159–1179.

[78] S.W. Walker, FELICITY: Finite ELement Implementation and Computational Interface Tool for You, http://www.mathworks.com/matlabcentral/fileexchange/31141-felicity.

[79] Y. Notay, An aggregation-based algebraic multigrid method, Electron. Trans. Numer. Anal. 37 (2010) 123–146.

[80] A. Napov, Y. Notay, Algebraic analysis of aggregation-based multigrid, Numer. Linear Algebra Appl. 18 (3) (2011) 539–564, http://dx.doi.org/10.1002/nla.741.

[81] A. Napov, Y. Notay, An algebraic multigrid method with guaranteed convergence rate, SIAM J. Sci. Comput. 34 (2) (2012) A1079–A1109, http://dx.doi.org/10.1137/100818509.

[82] Y. Notay, Aggregation-based algebraic multigrid for convection–diffusion equations, SIAM J. Sci. Comput. 34 (4) (2012) A2288–A2316, http://dx.doi.org/10.1137/110835347.

[83] G.H. Golub, C.F. Van Loan, Matrix Computations, 4th edition, Johns Hopkins University Press, Baltimore, MD, USA, 2013.

[84] S. Alama, L. Bronsard, X. Lamy, Analytical description of the Saturn-ring defect in nematic colloids, Phys. Rev. E 93 (2016) 012705, http://dx.doi.org/10.1103/PhysRevE.93.012705.

[85] E. VanderZee, A.N. Hirani, D. Guoy, E.A. Ramos, Well-centered triangulation, SIAM J. Sci. Comput. 31 (6) (2010) 4497–4523, http://dx.doi.org/10.1137/090748214.

[86] S. Walton, O. Hassan, K. Morgan, Strategies for Generating Well Centered Tetrahedral Meshes on Industrial Geometries, Springer International Publishing, Cham, 2015, pp. 161–180.

[87] A. Liu, B. Joe, Quality local refinement of tetrahedral meshes based on 8-subtetrahedron subdivision, Math. Comput. 65 (215) (1996) 1183–1200.

[88] S. Korotov, M. Křížek, Global and local refinement techniques yielding nonobtuse tetrahedral partitions, Comput. Math. Appl. 50 (7) (2005) 1105–1113, http://dx.doi.org/10.1016/j.camwa.2005.08.012, Numerical Methods and Computational Mechanics, http://www.sciencedirect.com/science/article/pii/S0898122105003391.

[89] N.J. Mottram, C.J.P. Newton, Introduction to Q-tensor theory, arXiv:1409.3542, 2014.

[90] Ennio De Giorgi, Selected Papers, 2006.

[91] S. Bartels, Stability and convergence of finite-element approximation schemes for harmonic maps, SIAM J. Numer. Anal. 43 (1) (2006) 220–238, http://www.jstor.org/stable/4101259.

[92] A. Braides, Local Minimization, Variational Evolution and Γ-Convergence, Lecture Notes in Mathematics, vol. 2094, Springer, 2014.

[93] G. Dal Maso, An Introduction to Γ-convergence, Progress in Nonlinear Differential Equations and Their Applications, vol. 8, Birkhäuser Boston Inc., Boston, MA, 1993.